Materials Today Bio 12 (2021) 100142

Contents lists available at ScienceDirect

Materials Today Bio

journal homepage: www.journals.elsevier.com/materials-today-bio

The spatial form periosteal-bone complex promotes bone regeneration by coordinating macrophage polarization and osteogenic-angiogenic events

C. Zhao [a,b,c], P. Qiu [a,b,c], M. Li [a,b,c], K. Liang [a,b], Z. Tang [a,b], P. Chen [a,b], J. Zhang [a,b], S. Fan [a,b,**], X. Lin [a,b,*]

[a] Department of Orthopaedic Surgery, Sir Run Run Shaw Hospital, Medical College of Zhejiang University, Hangzhou, China
[b] Key Laboratory of Musculoskeletal System Degeneration and Regeneration Translational Research of Zhejiang Province, China

ARTICLE INFO

Keywords:
Periosteal-bone complex
Macrophage polarization
Stiffness
Osteogenesis
Angiogenesis
Bone healing

ABSTRACT

Bone defects associated with soft tissue injuries are an important cause of deformity that threatens people's health and quality of life. Although bone substitutes have been extensively explored, effective biomaterials that can coordinate early inflammation regulation and subsequent repair events are still lacking. We prepared a spatial form periosteal bone extracellular matrix (ECM) scaffold, which has advantages in terms of low immunogenicity, good retention of bioactive ingredients, and a natural spatial structure. The periosteal bone ECM scaffold with the relatively low-stiffness periosteum (41.6 ± 3.7 kPa) could inhibit iNOS and IL-1β expression, which might be related to actin-mediated YAP translocation. It also helped to promote CD206 expression with the potential influence of proteins related to immune regulation. Moreover, the scaffold combined the excellent properties of decalcified bone and periosteum, promoted the formation of blood vessels, and good osteogenic differentiation (RUNX2, Col 1α1, ALP, OPN, and OCN), and achieved good repair of a cranial defect in rats. This scaffold, with its natural structural and biological advantages, provides a new idea for bone healing treatment that is aligned with bone physiology.

1. Introduction

At present, single-phase bone-centered substitutes with high stiffness (such as bioceramics and bioglasses) are widely utilized because of their resemblance to the mineral composition of bone [1]. These substitutes have superiority in osteogenic differentiation [2] but have limited effects on inflammatory regulation or angiogenesis [3,4]. Researchers have attempted to modify their properties, for example, by incorporatingchemical molecules and surface coatings to adjust the local microenvironment [5,6]. However, these types of artificial synthesis or single factor addition are dissimilar with natural conditions, and the specific dosage, presentation rate, and release process are difficult to control [3]. An ideal biomaterial is thought to be a dynamic control system that can coordinate early inflammatory regulation and subsequent angiogenic, osteogenic differentiation events [7].

It is known that complicated fractures are often accompanied by damage to adjacent soft tissues, which can aggravate the recruitment of macrophages to the injury site, and the persistence of inflammation is detrimental to fracture healing [8]. Studies have shown that the proportion of inflammatory cells increased significantly in both the soft tissue and bone hematoma after injury, but as the repair progresses, upregulation of antiinflammatory cytokines (such as IL-10) was more pronounced in the bone hematoma when comparing to that in the soft tissue hematoma [9,10]. Therefore, reasonable avoidance of inflammatory infiltration from soft tissues is potentially helpful for bone healing, but the inflammatory blockage is difficult to solve using simple bone-centered substitutes.

Natural bone is a highly vascularized stiff tissue coated with soft periosteum, which provides 30%–40% of the blood supply and delivers nutrients to the cortical bone [11,12]. The periosteum is a physical barrier that resists excessive penetration of inflammatory cells in traumatic environments and provides a supportive microenvironment for multifunctional mesenchymal stromal cells to accelerate bone remodeling [13]. Our previous study demonstrated that a periosteum-derived hydrogel could enhance M2 macrophage polarization in the early repair of bone injury [7]. And many researchers have reported the importance of preserving the periosteum in cortical healing in different animal models [14,15]. Given the advantages of natural periosteum in physical blockage, macrophage regulation, and angiogenesis, we

* Corresponding author.
** Corresponding author.
E-mail addresses: shunwu_fan@zju.edu.cn (S. Fan), xianfeng_lin@zju.edu.cn (X. Lin).
[c] These authors have contributed equally.

https://doi.org/10.1016/j.mtbio.2021.100142
Received 28 July 2021; Received in revised form 9 September 2021; Accepted 14 September 2021
Available online 17 September 2021

Abbreviation

IFN-γ	interferon-gamma
VEGF	vascular endothelial growth factor
PDGF	platelet-derived growth factor
BMP-2	bone morphogenetic protein 2
PBS	phosphate buffer solution
SDS	sodium dodecyl sulfate
RUNX2	runt-related transcription factor 2
Alp	alkaline phosphatase
Ocn	osteocalcin
Opn	osteoprotegerin
TNF-α	tumor necrosis factor-α
IL-1β	interleukin-1β
iNOS	inducible nitric oxide synthase
Arg1	arginase-1
IL-10	interleukin-10
OCT	optimal cutting temperature compound
AFM	atomic force microscopy
Micro-CT	micro-computed tomography
SEM	scanning electron microscope
EDS	energy-dispersive X-ray spectroscopy
qPCR	quantitative real-time polymerase chain reaction
LAT-A	latrunculin A
BMMs	bone marrow-derived macrophages
OI	osteogenic induction
MSCs	marrow mesenchymal cells
DB	decellularized bone scaffolds
DCB	decellularized decalcified cortical bone
DAPI	4′,6-diamidino-2-phenylindole
SD	standard deviation
ANOVA	one-way analysis of variance
NIH	national institutes of health

intended to prepare a natural spatial form periosteal-bone complex to regulate macrophage polarization in the early stage of injury and promote subsequent bone healing.

Macrophages play an important role in the early inflammatory regulation of bone healing. Under stimulation by interferon-gamma (IFN-γ), they differentiate into the M1 phenotype and participate in the removal of necrotic substances and amplification of inflammation [16]. Good bone repair requires timely termination of inflammation and conversion of M2 macrophages [17] because M2 macrophages can release biological signals through paracrine signaling to produce positive feedback on vascularization and mineralized deposits [6,18–20]. Recently, there has been a growing recognition that physical properties (such as stiffness) have a dramatic impact on macrophage phenotype [21]. It has been reported that macrophages are oriented to M2 polarization on low- or medium-stiffness gels and tend to M1 polarization on stiff gels [22]. However, the molecular mechanisms underlying the stiffness control of macrophage phenotypes are still poorly understood. Macrophages cannot directly perceive the stiffness of the substitutes they adhere to [23], actomyosin-mediated contractility and actin-mediated cytoskeleton reorganization are the main modulators for mechanical signal transduction [24]. A previous study demonstrated that macrophages adhered to a soft fibrin hydrogel had reduced inflammatory phenotypes compared to those adhered to a stiff hydrogel, which was associated with the decreased YAP nuclear localization resulting from the reduced cytoskeleton aggregation on the soft hydrogel [25]. Thus, we performed a preliminary exploration of the possible mechanism by which periosteal bone scaffold regulated the macrophage phenotype from the perspective of stiffness.

Actually, our group has been committed to the study of periosteal-related biomaterials in bone healing for many years. We reported the preparation of periosteal ECM scaffold in 2015 [26] and studied the mechanism of spontaneous mineralization of periosteal ECM scaffold [27]. We further found that the periosteal ECM gel has the potential to build a benign immune microenvironment at the early repair of bone defects [7]. These studies broadened our conventional understanding and application of the periosteum. In this study, we prepared the periosteal-bone complex by imitating the natural structure, and taking advantage of the native periosteum to make up for the shortcomings of the current single-phase bone-centered substitutes in macrophage regulation and vascularization, so as to better promote bone repair.

2. Materials and methods

Animal experiments in this study were conducted at the experimental animal center of Sir Run Run Shaw Hospital. All protocols were performed in accordance with the National Institutes of Health (NIH) guidelines and the Guidelines for Care and Use of Experimental Animals of Sir Run Run Shaw Hospital. The research protocols were approved by the Medical Ethics Committee of Sir Run Run Shaw Hospital.

2.1. Preparation of the periosteal bone scaffold

Femurs were isolated from large white swine at a local slaughterhouse with strict selection criteria (healthy male adult pigs of the same age, gender, and similar body weights), the muscle and adipose tissue attached to the surface of the femurs were separated with a scalpel. The harvested femoral shafts were further cut into pieces (10 mm in length, 6 mm in width, and 2 mm in thickness), washed with sterile phosphate buffer solution (PBS) three times, and stored in a refrigerator at −80 °C. The scaffolds were prepared with a two-step method, in brief, samples were first immersed in a 25% (w/v) EDTA-2Na solution (Macklin Biochemical Co., Ltd, Shanghai, China) and then decalcified in an ultrasonic rapid decalcifier (Pro-Cure Medical Technology Co., Ltd., Hong Kong, China) at 22 °C with a frequency of 40 kHz for 12 days, the decalcification solution was replaced every 2 days. After decalcification, the samples were treated with 1% (w/v) Triton X-100 (Sigma-Aldrich Corp., Saint Louis, USA) for 24 h, and then 1% (w/v) sodium dodecyl sulfate (SDS, Sigma-Aldrich Corp., Saint Louis, USA) for 2 h. For keeping the components and structure of the periosteum as intact as possible, the periosteum was wrapped with a barrier membrane (Solarbio, Beijing, China), while the cortical bone part was exposed to the 1% SDS solution for an additional 34 h. All decellularization processes were performed in an orbital shaker (Thermo Fisher Scientific, Wilmington, USA) at 4 °C under 100 rpm oscillation. Finally, all samples were washed with running double distilled water for 24 h and sequentially detoxified with 20 mM Tris-HCl (pH = 8.0) (Sigma-Aldrich, Saint Louis, USA) and 75% ethyl alcohol for 12 h, respectively, to remove residual SDS [28].

2.2. Scanning electron microscopy and energy-dispersive X-ray analyses

Scanning electron microscopy (SEM) was performed to observe the microstructure of the native and treated periosteal bone scaffolds. The samples were fixed in 2.5% (w/v) glutaraldehyde at 4 °C overnight and washed three times with PBS. Then, the samples were immersed in 1% (w/v) osmium tetroxide for 2 h and dehydrated in 50%, 70%, 80%, 95%, and 100% ethanol. After drying in hexamethyldisilazane (Macklin Biochemical Co., Ltd, Shanghai, China), they were coated with gold to a thickness of 25 nm under vacuum (K550, Emitech, London, UK) and immediately observed under a scanning electron microscope (TM-1000, Hitachi, Tokyo, Japan). Three different regions of bone parts were

selected for energy-dispersive X-ray spectroscopy (EDS, TM-1000, Hitachi, Tokyo, Japan) was performed to determine the distribution of calcium and phosphorus in the native and treated periosteal bone scaffolds.

2.3. Mechanical testing and atomic force microscopy analysis

The mechanical properties of the native and treated periosteal bone scaffolds were measured using a computer-controlled mechanical test machine (Z2.5, Zwick/Roell, Ulm, Germany). The scaffolds were placed flat on an operating table, and then the scaffolds were vertically compressed at a rate of 5 mm/min, and stress—strain curves based on loading force (F) and displacement (d) were recorded.

Atomic force microscopy (AFM; Icon, Veeco, USA) was used to obtain the high-resolution topography of the samples, mainly through interactions between a sharp probe and the samples. The samples were cut into pieces (width of 5 mm, length of 5 mm, and thickness of 1 mm) and placed on a clean mica sheet. For each sample, three 10 μm × 10 μm areas were selected for scanning. After calibration, high-resolution topography images were acquired. AFM was further used to measure the mechanical properties of the samples through nanoindentations. For each sample, force mapping was conducted on nine randomly selected regions with a peak force setpoint of 2 N for the periosteum part and 15 N for the cortical bone part to calculate Young's modulus.

2.4. Quantitative real-time polymerase chain reaction analysis

Quantitative real-time polymerase chain reaction (qPCR) analysis was performed to evaluate genes related to osteogenic differentiation and the macrophage phenotype. The total RNA of cells cultured on the scaffolds was extracted using a universal RNeasy kit (CWBIO, Beijing, China). The concentrations of the extracted RNA were measured at 260 and 280 nm using a Nanodrop 8000 spectrophotometer (Thermo Fisher, Billerica, USA). cDNA was synthesized according to the manufacturer's instructions. PCR amplification was performed in a reaction system containing 10 μL SYBR Premix, 1 μL each PCR upstream primer and PCR downstream primer, 1 μL cDNA template, and 7 μL ddH_2O. The expression of osteogenesis-related genes (*runt-related transcription factor 2, RUNX2; collagen 1α, Col1a1; alkaline phosphatase, Alp; osteocalcin, Ocn; osteoprotegerin, Opn*), M1 macrophage markers (*tumor necrosis factor-α, TNF-α; interleukin-1β, IL-1β; inducible nitric oxide synthase, iNOS*) and M2 macrophage markers (*CD206; arginase-1, Arg1; interleukin-10, IL-10*) were determined and normalized to that of β-actin (internal reference) using the $2^{-\Delta\Delta Ct}$ method. The analyzed gene sequences are detailed in Supplementary Table 1.

2.5. Immunofluorescence analysis

Immunofluorescence analysis was performed to verify the expression of osteogenic markers and macrophage-associated markers, as well as the expression and localization of YAP. Cells cultured on scaffolds were fixed with 4% paraformaldehyde for 20 min and washed twice with PBS. The nonspecific binding sites were blocked with 5% fetal bovine serum albumin (BSA) for 30 min. Then, the diluted primary antibodies of RUNX2 (1:1600; Cell Signaling Technology, Boston, USA), Col 1α1 (1:400; Cell Signaling Technology, Boston, USA), iNOS (1:400; Proteintech, Rosemount, USA), CD206 (1:400; Proteintech, Rosemount, USA) and YAP (1:100; Cell Signaling Technology, Boston, USA) were added and incubated overnight in the dark at 4 °C. According to the origin of the primary antibodies, the corresponding secondary antibodies were selected for further incubation. DAPI (4′,6-Diamidino-2-phenylindole, 1:100; Solarbio, Beijing, China) was used to stain the nuclei for 15 min at room temperature and Phalloidin-iFluor 555 (1:1000; Abcam, Cambridge, UK) was used to stain the cytoskeleton for 30 min under the same conditions. The specimens were observed by using a confocal microscope (Nikon, Tokyo, Japan).

2.6. Mouse skeletal muscle–femur injury model

A mouse skeletal muscle–femur injury model, was aimed to determine the macrophage infiltration in the surrounding tissue at the inflammatory stage. Twenty-four healthy 8-week-old male C57BL/6 mice were fed with sufficient water and food in a 12 h light/12 h dark cycle at 23 ± 3 °C. After a week of adaptation, they were intraperitoneally anesthetized with 40 mg/kg 1% pentobarbital sodium. For creating the soft tissue–femur injury model, similar published procedures were followed [7,29]. In short, a 0.5 mm hole was made using a fine surgical burr at the middle of the femur condyles, and a stainless-steel pin was inserted into the intramedullary canal of the femur. Then, a 50% depth femur segmental defect 2 mm long was created at the middle of the femur. The quadriceps around the defect were cut at 75% of the width and 50% of the thickness. The soft tissue–femurs were harvested at one, three, and seven days after surgery for flow cytometry and immunofluorescence analysis.

2.7. Subcutaneous implantation

For the angiogenic evaluation, healthy male BALB/c nude mice (4–6 weeks old, n = 8) were fed under the conditions mentioned above and divided into two groups for subcutaneous implantation. First, the decellularized decalcified cortical bone (DCB, n = 4) and periosteal bone scaffolds (n = 4) were processed into 5 mm × 5 mm × 1 mm pieces. After disinfection with iodophor and anesthetization with 1% pentobarbital sodium 40 mg/kg, a 5 mm longitudinal incision was made on the back of each nude mouse. A vascular clamp was used to perform inert separation under the skin to form a cavity, in which the scaffolds were implanted with sterile forceps. Finally, the incision was closed with a 4–0 absorbable suture (Jinhuan Medical Products Co., Ltd, Shanghai, China), and the surgical area was disinfected with iodophor. After feeding for 4 weeks, all mice were anesthetized to death with 40 mg/kg 3% pentobarbital sodium, and scaffolds were harvested for analysis. The immune response of the DCB and periosteal bone scaffolds after subcutaneous implantation was also explored. Healthy male Sprague-Dawley rats (6–8 weeks old, n = 8) were divided into two groups, and the surgical method was similar to that described above. They were anesthetized to death seven days after surgery, and subcutaneous capsular tissues were collected for analysis.

2.8. Rat cranial bone defect model

Thirty-six healthy adult male Sprague-Dawley rats (weighing 200–250 g, 6–8 weeks old) were used for cranial regeneration. They were divided into three groups, an empty defect group (n = 12), a DCB group (n = 12) and a periosteal bone group (n = 12). All of them were fed under the conditions mentioned above. After anesthetization, they were placed on a surgical plate in a prone position, and their heads were fixed to expose the surgical area. After disinfecting twice with iodophor and covering the surgical areas with sterile scarves, 2 cm incisions were made, and full-thickness critical-sized calvarial defects were created in the central zone with a cyclovergence (Precision Tools Co., Ltd., Shanghai, China). The corresponding scaffolds were implanted to fill in the defect areas with the periosteum on top. Finally, the scalps were closed with 4–0 absorbable sutures, and penicillin was injected continuously for 2 days to prevent infection.

2.9. Flow cytometry

Cells from the bone marrow and muscle were collected on days 1, 3, and 7 to assess changes of macrophage phenotype in the skeletal muscle–femur injury model. Cells in the femur bone marrow were flushed out by PBS with a 1 mL syringe, the supernatants were discarded after centrifugation at a speed of 1500 G/min, and the remaining cells were incubated with erythrocyte lysis buffer for 10 min at room

temperature to lyse the erythrocytes. Samples were then collected by centrifugation for subsequent staining. The collection of cells from the muscles required chopping of the muscle until there were no visible particles. The mixtures were digested with 2 μg/mL collagenase (Sigma-Aldrich Corp., Saint Louis, USA) for 30 min at 37 °C, filtrated with a 40 μm strainer (BD Biosciences, New York, USA), and washed with PBS. Then, cell suspensions were collected and further digested with trypsin (Sigma-Aldrich Corp., Saint Louis, USA) for 10 min at 37 °C to yield the single-cell suspensions. After blocking with 5% BSA for 30 min, cells collected from the bone marrow and muscles were incubated with primary antibodies against ACP-conjugated CD11b (1:80; Biolegend, San Diego, USA), FITC-conjugated CD45 (1:200; Biolegend, San Diego, USA) and PE-conjugated Ly6C (1:320; Biolegend, San Diego, USA) at 4 °C for 30 min in the dark. Cells were washed with PBS to remove excess antibodies and resuspended in 300 μL PBS for test using a FACSCalibur flow cytometer (BD Biosciences, New York, USA) and CellQuest software; all data were analyzed using Flow Jo software.

Cells from the subcutaneous capsular were also obtained to evaluate the macrophage phenotype in the subcutaneous implantation models on day 7. In brief, the capsular was chopped up until there were no visible particles, then digested with 2 μg/mL collagenase for 30 min at 37 °C, and filtrated with a 40 μm strainer, and further digested with trypsin for 10 min at 37 °C. The collected cells were treated with Percp-conjugated F4/80 (1:40; Biolegend, San Diego, USA), PE-conjugated CD11c (1:160; Biolegend, San Diego, USA) and FITC-conjugated CD206 (1:400; Biolegend, San Diego, USA) for further testing.

2.10. In vivo histological analysis

Immunofluorescence was conducted to evaluate the inflammatory cells infiltration and macrophage polarization surrounding the defect site in the skeletal muscle–femur injury model and the cranial bone defect model on day 7. After decalcification, the specimens were embedded in an optimal cutting temperature compound (OCT) (Solarbio, Beijing, China) and cut into slices with a thickness of 7 μm using a freezing microtome (CM1950, Leica, Wetzlar, Germany). Antigen retrieval was performed with a 1 × citrate antigen retrieval solution (Solarbio, Beijing, China) at 65 °C overnight. After rinsing with PBS three times, the primary antibodies iNOS (1:400; Proteintech, Rosemount, USA), CD86 (1:200; Cell Signaling Technology, Boston, USA), and CD206 (1:400; Proteintech, Rosemount, USA) were incubated at 4 °C in the dark overnight. Then, the corresponding secondary antibody was added to the slices for specific binding, and the nucleus was stained with DAPI for 10 min at room temperature. Finally, the stained slices were photographed using a confocal microscope (Nikon, Tokyo, Japan).

Histological analysis was performed to evaluate bone regeneration. All cranium specimens were fixed in 4% paraformaldehyde for 24 h and decalcified with 25% (w/v) EDTA-2Na in an ultrasonic rapid decalcifier (Pro-Cure Medical Technology Co., Ltd., HongKong, China) for 7 days. After gradient dehydration, the specimens were embedded in paraffin and cut into 7 μm slices. H&E staining (Jiancheng Technology Co., Ltd, Nanjing, China) was performed, and all slides were observed under an optical microscope (Nikon, Tokyo, Japan).

2.11. Statistical analysis

Data in this study are expressed as mean ± standard deviation (SD). Statistical analyses were performed using one-way analysis of variance (ANOVA) and unpaired Student's *t*-test by SPSS 19.0. Statistical significance was set at $P < 0.05$.

2.12. Other experimental methods

Other experimental methods in this study were detailed in the supplementary data.

3. Results

3.1. Inflammatory cells accumulated around the injury site and impaired adjacent osteogenesis

When a fracture occurs, large numbers of inflammatory cells from circulating blood, surrounding muscles, and internal bone marrow infiltrate into the defective area. The periosteum acts as a physical barrier that may help prevent excessive infiltration of inflammatory cells from the muscle. A skeletal muscle–bone injury model was constructed to evaluate changes in distribution and quantity of inflammatory cells in the muscle and bone marrow around the injured area. Flow cytometry results showed that the proportion of inflammatory cells ($CD45^{+}CD11b^{+}Ly6C^{+}$) in the bone marrow gradually decreased from 36.7% (day 1) to 10.1% (day 7), but the proportion in the muscle maintained at a high level (from 31.8% on day 1–22.3% on day 7) (Fig. 1A). Immunofluorescence revealed that cells in both the muscle and bone marrow around the injured area positively expressed iNOS (M1 macrophage markers) on the first day, and they gradually decreased by the seventh day (Fig. 1B). These results suggest that inflammatory cells accumulated around the injury site, and inflammation in the muscle area subsided relatively slowly. Then, an injured skeletal muscle model was used to evaluate whether it affected the adjacent osteogenic differentiation of primary osteoblasts. After culturing for 7 days, less alkaline phosphatase and weaker alizarin red staining were observed in the injured group compared to those in the osteogenic induction (OI) group (Fig. 1C). The expression of osteogenic genes (*RUNX2, ALP, Col 1α1, OCN,* and *OPN*) was elevated in the injured group compared with those in the control group, but all of them were markedly lower than those in the OI group (*RUNX2*, *ALP*, *Col 1α1*, and *OCN:* $P < 0.05$; *OPN:* $P > 0.05$) (Fig. 1D), this suggests that muscles damage has potential to affect adjacent osteogenesis (the schematic diagram was Fig. 1E). Based on these results, we proposed to prepare the spatial form periosteal bone scaffold to reasonably avoid inflammatory infiltration from skeletal muscles.

3.2. Evaluation of the spatial form periosteal bone scaffold

The periosteal bone scaffolds were prepared to limit inflammatory infiltration, in which the periosteum functioned as a barrier. After decellularization, the periosteal bone scaffold was assessed by histological staining and by DNA content and fragment size measurements. Compared with the native scaffolds, H&E and DAPI staining demonstrated that the nuclei were effectively eliminated from the periosteal bone scaffolds (Fig. 2A). There were no noticeable DNA bands in either the bone or periosteum part in the agarose gel separation experiments (Suppl. Fig. 1C), and the DNA contents were significantly reduced from 97.4 ± 14.6 ng/mg dry weight to 8.2 ± 3.0 ng/mg in the cortical bone part ($P < 0.05$) and from 1739.0 ± 108.9 ng/mg to 30.7 ± 14.0 ng/mg in the periosteum part ($P < 0.05$) (Fig. 2B). Micro-computed tomography (micro-CT) was performed to evaluate decalcification, revealing that mineralized elements were completely removed (Suppl. Fig. 1B). Therefore, the periosteal bone scaffolds met the decellularization standards and were well decalcified.

3.3. The spatial form periosteal bone scaffold retained main biological components and possessed a complete three-dimensional structure

Picrosirius red staining and polarized light observation were used to assess collagen alignment and structure. Although collagens in the native scaffold were slightly deeper than those in the periosteal bone scaffold, their distributions were similar (Fig. 2C). The collagen contents in both the periosteum and bone part slightly decreased, but there were no significant differences between the native and the treated scaffolds in the periosteum part, as well as in the bone part (Fig. 2D, $P > 0.05$). The contents of GAGs in both the periosteum and bone part were lower than that in the native scaffolds (Fig. 2E, $P < 0.05$). Overall, the main

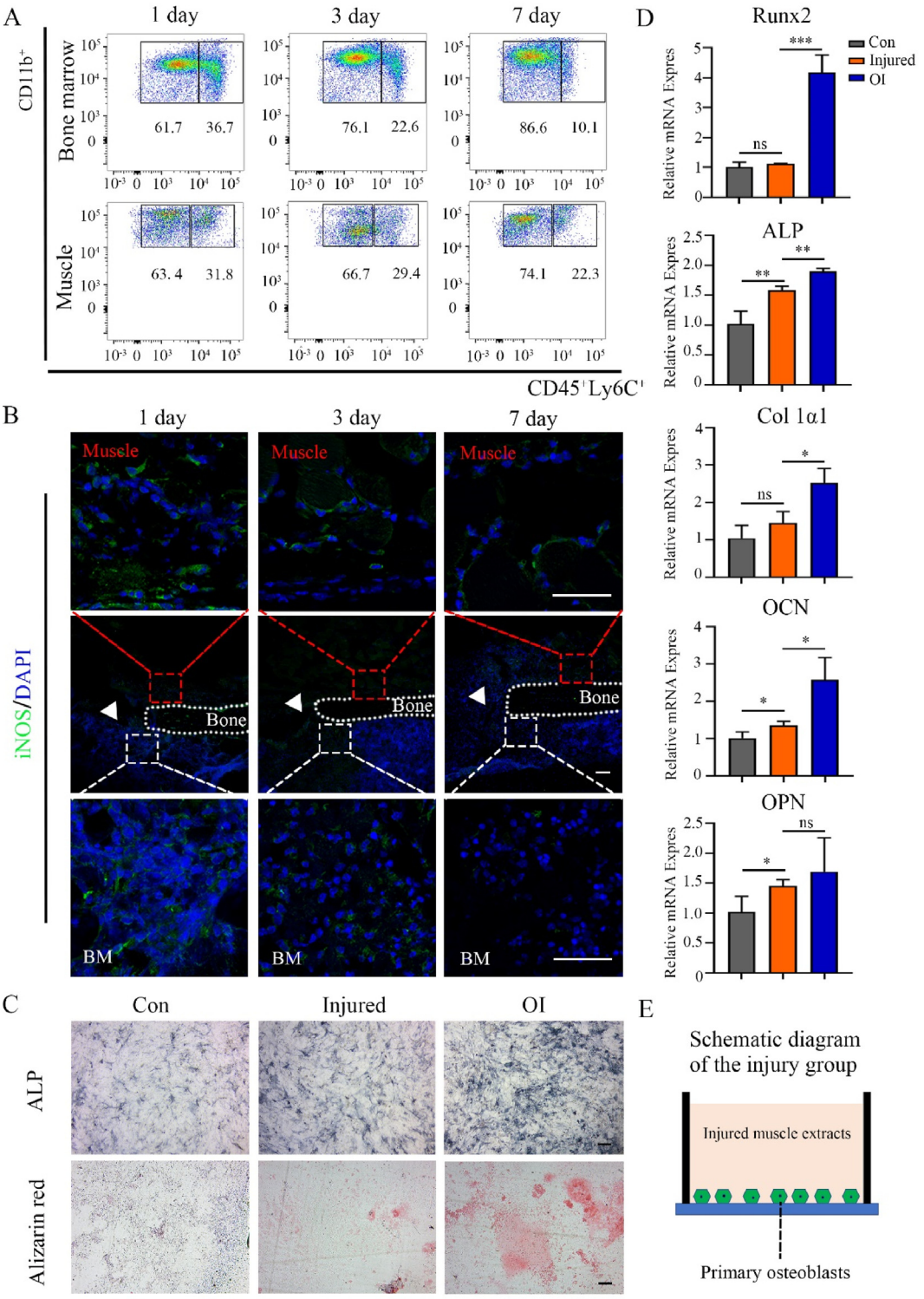

Fig. 1. Infiltration of inflammatory cells around the skeletal muscle–femur injury site and the influence of injured skeletal muscles on osteogenesis. (A) Representative flow cytometry analysis to examine the changes in the number of CD45, CD11b, and Ly6C positive cells in the muscles and bone marrow at the injury site from day 1 to day 7. (B) Representative immunofluorescence staining of iNOS positive cells around the injured site from day 1 to day 7 (green: iNOS; blue: cell nucleus; red box: surrounding muscle; white box: bone marrow; white triangle: defect area; BM: bone marrow). (C) Alkaline phosphatase and alizarin red staining of primary calvarial osteoblasts in the control, injured, and osteogenic induction (OI) groups. (D) Relative mRNA expression of *RUNX2, ALP, Col 1α1, OCN,* and *OPN* from primary calvarial osteoblasts in the control, injured, and OI groups after culturing for 7 days. (E) Schematic diagram of osteogenic induction in the muscle injury group. Data are presented as mean ± SD (n = 4). (Scale bar = 100 μm; *: $P < 0.05$, **: $P < 0.01$, and ***: $P < 0.001$).

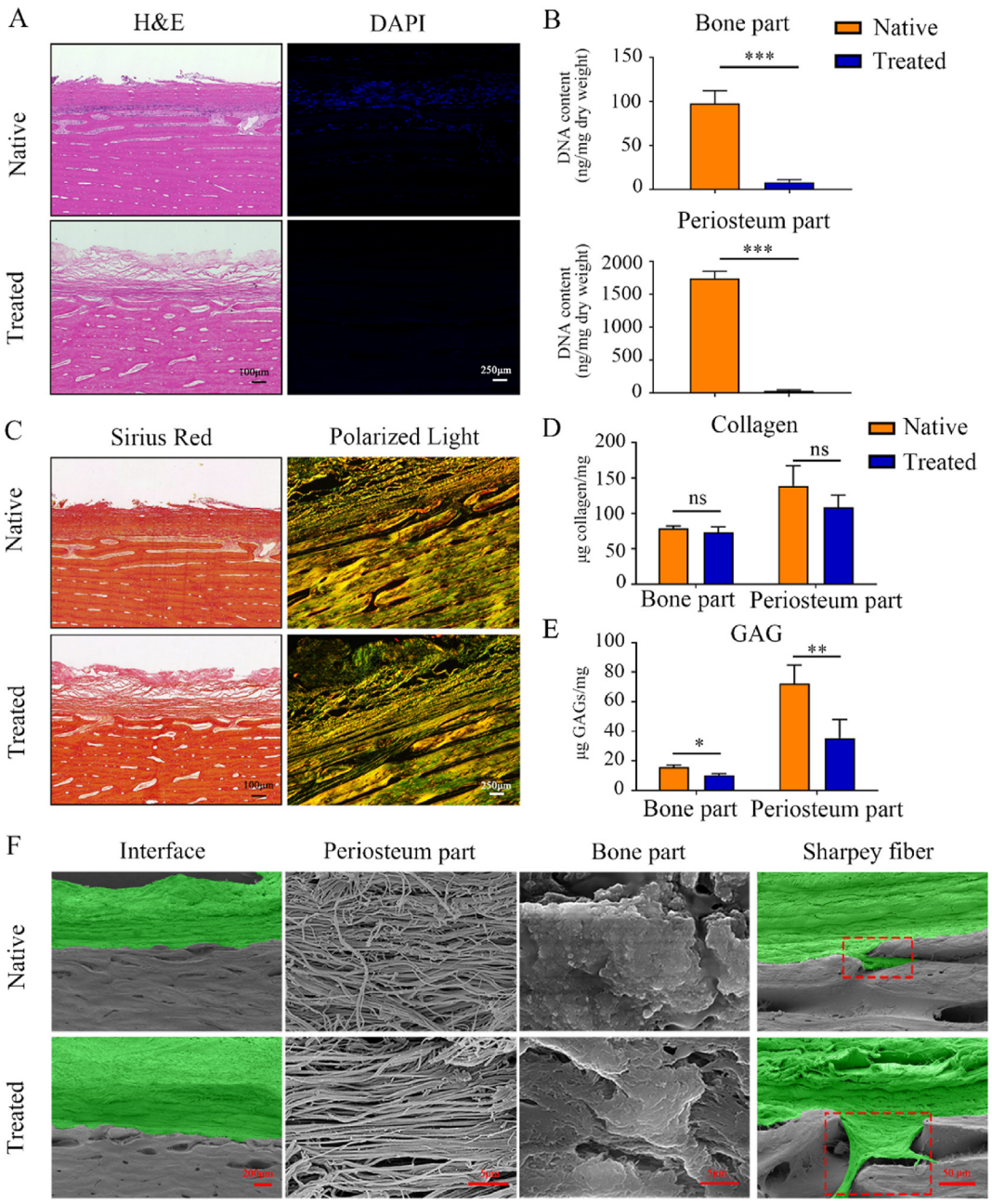

Fig. 2. Validation of the spatial form periosteal bone ECM scaffold and three-dimensional structure evaluation. (A) H&E and DAPI staining of the native and treated periosteal bone ECM scaffolds. (B) DNA contents of the periosteum part and cortical bone part before and after treatment. (C) Sirius red staining and polarized light microscopy observations of the types and orientations of collagen in the native and treated periosteal bone ECM scaffold. (D, E) Collagen (D) and GAGs (E) contents in the periosteum part and cortical bone part before and after treatment. (F) Scanning electron microscopy (SEM) images of the periosteum part, cortical bone part, interfaces, and Sharpey fibers of the native and treated periosteal bone ECM scaffolds (green: periosteum; gray: cortical bone; red dotted frame: Sharpey fiber). Native: before treatment; Treated: after treatment. Data are presented as mean ± SD (n = 4). (Scale bars are listed above; *: $P < 0.05$, **: $P < 0.01$, and ***: $P < 0.001$).

biological components of the periosteal bone scaffolds were preserved after decellularization and decalcification.

SEM images of the periosteal bone scaffolds showed a biphasic microarchitecture (Fig. 2F). It was noteworthy that Sharpey fibers (the special structure at the interface) were completely preserved (Fig. 2F). Collagens in the periosteum part tended to be dense and disordered in the native scaffolds but became loose and well oriented after treatment (Fig. 2F). The bone part had a crystal-like form, and there were no significant changes in the morphology before and after processing (Fig. 2F); however, energy-dispersive X-ray spectroscopy (EDS) analysis revealed that the calcium and phosphorus contents were significantly reduced (Suppl. Fig. 1D and E; $P < 0.05$). These evidences indicate that the three-dimensional structures of the periosteal bone scaffold were completely retained in the absence of calcium and phosphorus.

3.4. The periosteal bone scaffold possessed different physical, mechanical properties in the periosteum and cortical bone part

The mechanical properties of the periosteal bone scaffold before and after treatment were assessed, and the stress–strain curves were recorded. The stress-strain curves of both scaffolds were approximately J-shaped, but there were brief plateauing periods, which were indicative of

the biphasic structure of the scaffolds. The portion of the curves before the plateau mainly reflected the mechanical properties of the periosteum, while that after the plateau reflected mechanical properties of the cortical bone (Fig. 3A). The physical differences between the periosteum and cortical bone of the periosteal bone scaffolds were evaluated using AFM, cord-like fibrous structures were observed in the periosteum part (Fig. 3B), and granular, crystalline structures were observed in the cortical bone part (Fig. 3C). Nanoindentation test further reflected the mechanical properties of the periosteal bone scaffolds. The slope of the treated periosteum curve was significantly lower than that of the native periosteum, but there was no significant difference in the slopes of the native and treated cortical bone curves (Fig. 3D and E). The regional distribution of Young's modulus was also presented (Fig. 3F and G); its variation was similar to that of the nanoindentation test. Specifically, Young's modulus of the periosteum part decreased from 75.4 ± 5.5 kPa to 41.6 ± 3.7 kPa after treatment ($P < 0.05$), while no significant change was observed in the cortical bone part (1426 ± 77.9 kPa vs. 1375.8 ± 137.5 kPa, $P > 0.05$) (Fig. 3H).

3.5. The Periosteal bone scaffold inhibit M1 polarization might through actin-mediated YAP translocation

Bone marrow-derived macrophages (BMMs) were culture on the DCB and the periosteal bone scaffolds to evaluate their effects on macrophage

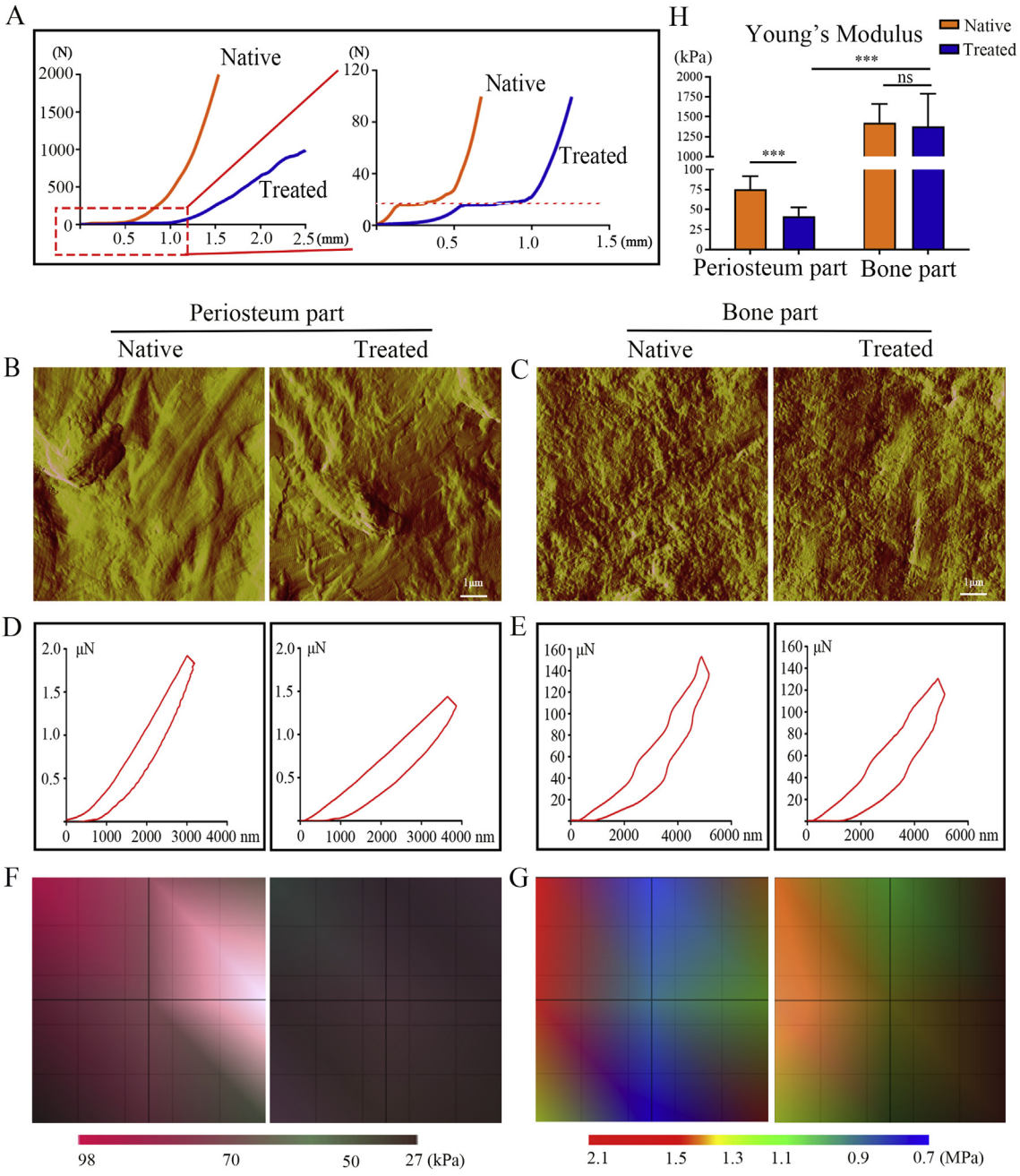

Fig. 3. Mechanical properties of the spatial form periosteal bone ECM scaffold before and after treatment. (A) Representative stress–strain curves of the periosteal bone ECM scaffold before and after treatment. (B, C) Representative atomic force microscopy images of the periosteum (B) and cortical bone part (C) before and after treatment. (D, E) Representative nanoindentation curves of the periosteum (D) and cortical bone part (E) before and after treatment. (F, G) Distribution maps of Young's modulus of the periosteum (F) and cortical bone part (G) before and after treatment. (H) Values of Young's modulus in the periosteum and cortical bone part before and after treatment. Native: before treatment; Treated: after treatment. Data are presented as mean ± SD (n = 4). (Scale bar = 1 μm; *: $P < 0.05$, **: $P < 0.01$, and ***: $P < 0.001$).

polarization. Immunofluorescence revealed that BMMs on the DCB scaffolds positively expressed iNOS, but almost no positive cells were observed on the periosteal bone scaffolds (Fig. 4A and B). The expressions of *IL-1β, TNF-α,* and *iNOS* in BMMs were analyzed at the gene level by qPCR after culturing for 24 h. Compared to the DCB group, the amounts of *IL-1β* and *iNOS* significantly decreased in the BMMs seeded on the periosteal bone scaffolds (Fig. 4C, D, $P < 0.05$). The amount of *TNF-α* also decreased, but the difference was not statistically significant (Fig. 4E, $P > 0.05$). These results suggest that the periosteal bone scaffold could inhibit the M1 polarization of macrophages.

The periosteum part and cortical bone part had different stiffnesses (Fig. 3H), and YAP has been shown to be related to mechanical

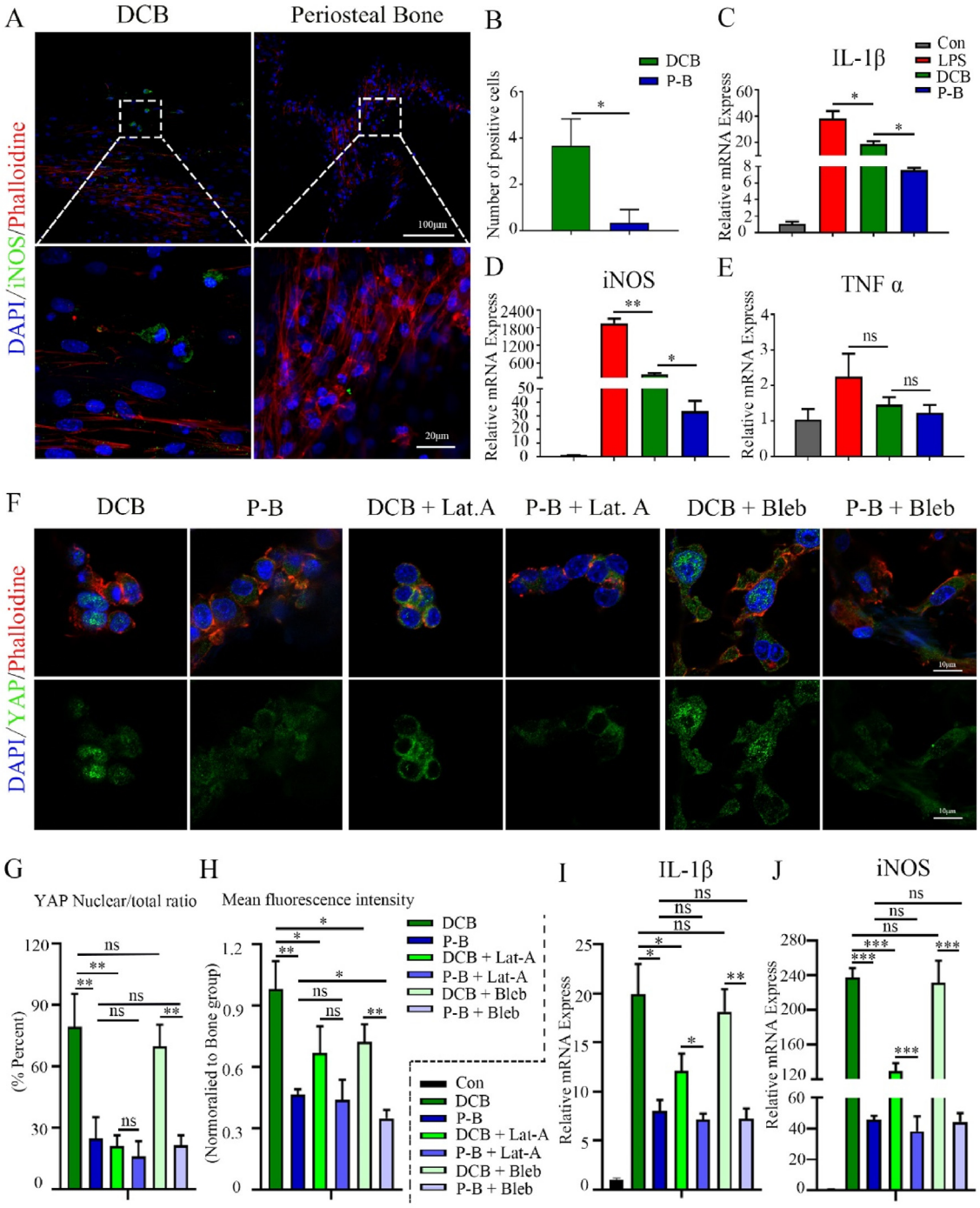

Fig. 4. Periosteal bone scaffold inhibits M1 polarization might through actin-mediated YAP translocation. (A) Representative immunofluorescence images of iNOS in BMMs cultured on DCB and the periosteal bone scaffolds for 24 h (green: iNOS; red: phalloidin, blue: nucleus; 20× and 80×). (B) Quantitative analysis of iNOS positive cells cultured in the same conditions as those in (A). (C, D, E) Relative mRNA expression of *IL-1β* (C), *iNOS* (D), and *TNF-α* (E) in BMMs cultured in the same conditions as those in (A). (F) Representative immunofluorescence images of YAP in BMMs cultured on DCB and the periosteal bone scaffold for 24 h and treated with LAT. A or blebbistatin for 6 h (green: YAP; red: phalloidin; blue: nucleus). (G) Quantitative analysis of YAP nuclear/total ratio in BMMs in (F). (H) Mean fluorescence intensity of YAP in BMMs in (F); the values were normalized to the DCB group. (I, J) Relative mRNA expression of *IL-1β* (I) and *iNOS* (J) in BMMs cultured on DCB and the periosteal bone scaffold for 24 h and treated with LAT. A or blebbistatin for 6 h. LPS: lipopolysaccharide; DCB: Decellularized decalcified bone scaffold; P–B: Periosteal bone scaffold. Data are presented as mean ± SD (n = 4). (Scale bars are listed above; *: $P < 0.05$, **: $P < 0.01$, and ***: $P < 0.001$).

transduction and inflammation regulation [30]; thus, YAP expression and its nuclear translocation were evaluated to explore the possible regulatory mechanism of macrophage polarization on composite periosteal bone scaffolds and single-phase DCB scaffolds. A higher mean fluorescence intensity and nuclear localization of YAP was found in the BMMs cultured on the stiffer DCB scaffold compared to those on the composite periosteal bone scaffolds (Fig. 4F, G, H), suggesting that YAP activity might be related to substrate stiffness. Latrunculin A (LAT. A, an inhibitor of actin polymerization) and blebbistatin (an inhibitor of myosin phosphorylation) were chosen to explore the association between YAP and the cytoskeleton. The application of LAT. A reduced YAP nuclear localization, but blebbistatin had little effect (Fig. 4F, G, H). Moreover, the expression of *IL-1β* and *iNOS* was also inhibited in BMMs cultured on stiffer DCB after LAT. A treatment (Fig. 4I and J), These data suggest that the composite periosteal bone scaffold was less likely to induce YAP nuclear localization compared to single-phase cortical bone and that inhibition of actin-mediated YAP nuclear translocation might be related to inflammation suppression.

3.6. The periosteal bone scaffold promoted M2 polarization and presented a benign repair microenvironment

For determining whether the periosteal bone scaffold could promote M2 polarization, the macrophage was analyzed by immunofluorescence. After culturing for 24 h, BMMs seeded on the periosteal bone scaffold clearly expressed CD206, while those on the cortical bone did not (Fig. 5A and B). The mRNA expression of M2 macrophage markers (*CD206, Arg1, and IL-10*) was significantly higher in the BMMs seeded on periosteal bone scaffold than in those on DCB scaffolds (Fig. 5C, D, E; $P < 0.05$). Therefore, the periosteal bone scaffold has the potential to induce M2 polarization of macrophages.

Proteomic analysis was conducted to investigate potential molecules related to macrophage polarization. AZU1, IGHG, and BGN were found in the periosteal bone scaffold, which might be related to immune regulation and assist M2 polarization (Fig. 5F); however, the exact mechanisms require further study. The proteomic analysis also revealed the possible molecules related to vascularization (PTN, Col 6A1, and HSPG2), osteogenesis (OGN), collagen assembly (BGN), and mineralization (SPP1, PHEX, ASPN, and SPARC) (Fig. 5F). Moreover, proteins related to cell components, molecular functions (including calcium binding, collagen binding, cell adhesion, protein-containing complex and integrin binding, and extracellular matrix structural constituents), and biological processes (including regulation of cell adhesion, proliferation and migration, ossification, regulation of angiogenesis, and extracellular matrix organization) might have a contribution to building a benign microenvironment for regeneration (Fig. 5G, H, I).

3.7. The periosteal bone scaffold facilitated osteogenic differentiation and angiogenesis

The osteogenesis properties of the periosteal bone scaffold were evaluated by assessing the expression of *RUNX2* on day 7 and *Col 1α1* on day 14 in bone marrow mesenchymal cells (MSCs) seeded on DCB and the periosteal bone scaffolds. Immunofluorescence showed that both the DCB and periosteal bone scaffold promoted the positive expression of *RUNX2* and *Col1a1* (Fig. 6A and B). The expression of osteogenesis-related markers (*RUNX2, Alp, Col 1α1, Opn*, and *Ocn*) was also verified by qPCR. These genes were significantly upregulated on day 14 in the MSCs seeded on the DCB and periosteal bone scaffold compared to those cultured on polystyrene (Fig. 6C). These results indicate that both DCB and periosteal bone scaffolds could facilitate osteogenic differentiation.

Next, the angiogenic ability of the periosteal bone scaffold was evaluated using Matrigel tube formation assay. Compared to the PBS and DCB groups, extracts from the periosteal bone scaffold induced more HUVEC tube-like structures (Fig. 6D). And the number of loops and branching points was significantly higher than those in the PBS and DCB groups ($P < 0.05$), but lower than that in the VEGF-induced group ($P < 0.05$) (Fig. 6E and F). Subcutaneous implantation of DCB and the periosteal bone scaffolds was performed to analyze the infiltration of blood vessels. Many blood vessels permeated the subperiosteal bone in the periosteal bone group, but there was almost no noticeable blood vessel infiltration in the DCB groups (Fig. 6G and H). These results demonstrate that the periosteal bone scaffold facilitates angiogenesis and blood vessel infiltration.

3.8. The periosteal bone scaffold exhibited good macrophage regulation at the subacute stage of implantation

Generally, implantation of substitutes induces inflammatory response at the early stage, which gradually subsides at the later subacute stage with macrophage phenotype transformation. In this study, CD86 and CD206 staining was applied to identify the macrophage infiltration at the subacute stage (day 7) of implantation. CD86 positive macrophages aggregated at the defect area in the empty defect group and DCB group, indicating the failure of M1-to-M2 conversion (Fig. 7A and B). In the periosteal bone scaffold group, almost no CD86 positive cells were observed (Fig. 7A and B), the CD206 positive macrophages were identified, which were mainly distributed around the periosteum region (Fig. 7A, C). The immune response of the DCB and periosteal bone scaffolds 7 days after subcutaneous implantation was also explored. Flow cytometry results showed that the proportion of $F4/80^{+}CD11c^{+}$ macrophages around the periosteal bone scaffolds was lower than that of DCB scaffolds (percentage of positive cells in $F4/80^{+}$ cells; DCB: 47.4%, periosteal bone: 28.0%), while the proportion of $F4/80^{+}CD206^{+}$ macrophages was higher than that of the DCB group (percentage of positive cells in $F4/80^{+}$ cells; DCB: 30.0%, periosteal bone: 52.8%) (Fig. 7D). These results suggest that the periosteal bone scaffold may have the potential to regulate macrophage polarization at the subacute stage of implantation by promoting the M1-to-M2 transformation timely.

3.9. The periosteal bone scaffold accelerated bone healing in vivo

For demonstrating the potential of the periosteal bone scaffold to accelerate bone regeneration, cranial bone defects were evaluated by micro-CT scan and histological analysis 4 and 8 weeks after implantation. As Fig. 8A showed, newly formed bone tissue was observed in all groups, but the amount of new bone varied among the three groups. The bone mineral density (BMD) and bone volume/total volume (BV/TV) values in the periosteal bone scaffold group were significantly higher than those in the defect and DCB groups (Fig. 7B and C). H&E staining detected noticeable defects in the empty defect group at both 4 and 8 weeks (Fig. 8D). In the DCB group, the defect was obvious after 4 weeks, but the newly generated bone was able to connect the scaffold to the host after 8 weeks (Fig. 8D). In the periosteal bone group, the periosteum was significantly degraded after 8 weeks; however, many blood vessels infiltrated the cortical bone surface, and reconnection of the defect was observed (Fig. 8D). In general, the periosteal bone scaffold promotes osteogenesis and angiogenesis, accelerating the healing of bone defects.

4. Discussion

In this study, we prepared a spatial form periosteal bone ECM scaffold, which coordinated macrophage polarization and promoted bone healing. Specifically, the periosteal bone ECM scaffold had the advantages of low immunogenicity, natural bioactive ingredients, and spatial structure. The periosteal bone ECM scaffold could inhibit M1 macrophage polarization by covering the relatively low-stiffness periosteum, which might be regulated by actin-mediated YAP translocation. It also promoted the M2 conversion of macrophages with the potential influence of proteins related to immune regulation. The effective regulation of early inflammation helped to reshape the local microenvironment, provided positive feedback for subsequent bone healing events, and promoted periosteal bone scaffold to

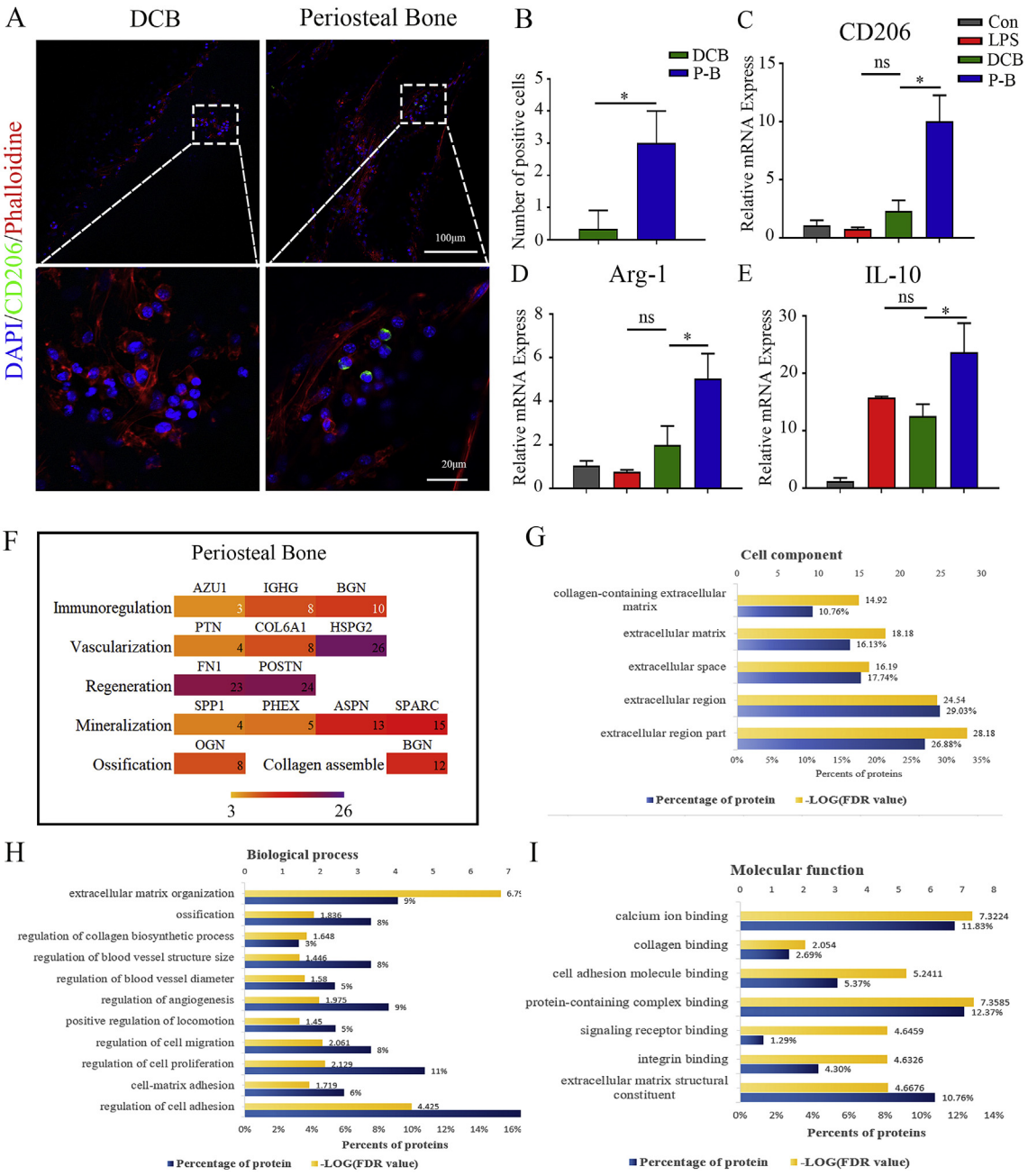

Fig. 5. The periosteal bone scaffold promoted M2 polarization and presented a benign repair microenvironment. (A) Representative immunofluorescence images of CD206 in BMMs cultured on DCB and the periosteal bone scaffolds for 24 h (green: CD206; red: phalloidin; blue: nucleus; 20 × and 80 ×). (B) Quantitative analysis of CD206 positive cells cultured in the same conditions as those in (A). (C, D, E) Relative mRNA expression of *CD206* (C), *Arg-1* (D), and *IL-10* (E) in BMMs cultured in the same conditions as those in (A). (F) Proteins that might be involved in immune regulation, vascularization, and regeneration in the periosteum, and proteins that might participate in mineralization, ossification, and collagen assembly in cortical bone. (G, H, I) Mass spectrometry results of the periosteal bone scaffold in aspects of cell components (G), biological process (H), and molecular functions (I). LPS: lipopolysaccharide; DCB: Decellularized decalcified bone scaffold; P–B: Periosteal bone scaffold. Data are presented as mean ± SD (n = 4). (Scale bars are listed above; *: $P < 0.05$, **: $P < 0.01$, and ***: $P < 0.001$).

perform the functions of osteogenesis and angiogenesis. Finally, the spatial form periosteal bone scaffold was proved to promote effective bone healing in the rat cranial defect model.

Currently, bone defects associated with soft tissue injuries are still a major disease affecting human health and incur large medical expenses [31,32]. In this study, inflammatory cells were observed in the soft tissue surrounding the defect area (Fig. 1B), and the decrease of inflammatory cells in muscle was less pronounced than that in bone marrow (Fig. 1A), which is similar to a previous report [9]. One possible reason is that the bone marrow environment with the surrounding periosteum and cortical bone had better prerequisites for regeneration than muscle. However, current widely used single-phase inorganic biomaterials provide relatively limited inflammatory regulation [3,4]. With increased awareness of the importance of the periosteum and the emergence of various artificial periosteal substitutes, its remarkable abilities for immune regulation and regeneration have become increasingly prominent [7,26,33]. Therefore, we prepared the periosteal bone scaffold to avoid excessive infiltration of inflammatory cells derived from soft tissue and to coordinate early inflammatory and subsequent osteogenesis, angiogenesis events by imitating natural bone repair mechanisms.

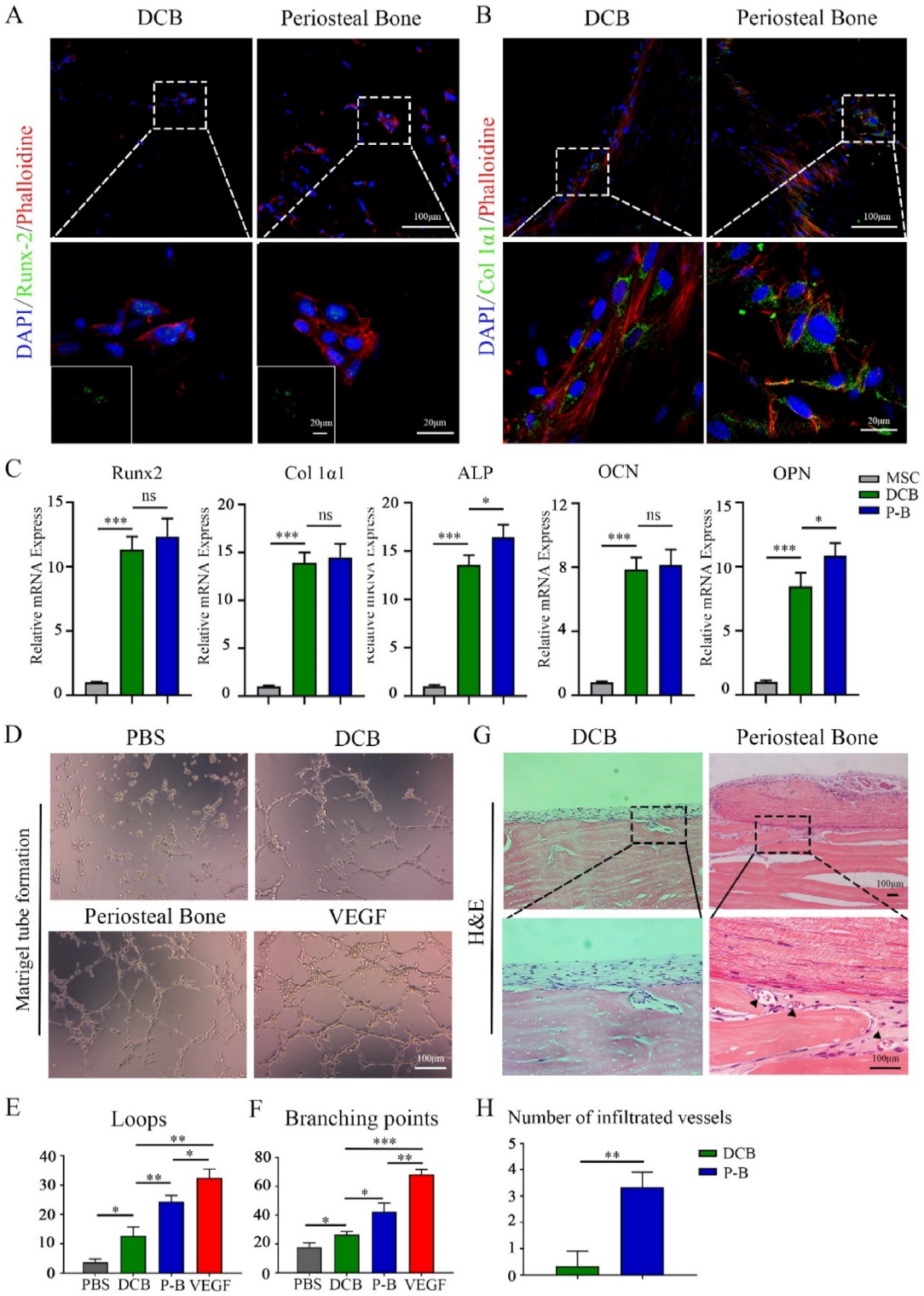

Fig. 6. The spatial form periosteal bone scaffold promoted osteogenesis and angiogenesis. (A, B) Representative immunofluorescence images showing the expression of RUNX2 (A) and Col 1α1 (B) in the MSCs cultured on the decellularized decalcified cortical bone (DCB), and periosteal bone scaffold for 7 and 14 days respectively (green: RUNX2 or Col 1α1; red: phalloidin; blue: nucleus). (C) Relative mRNA expression of *RUNX2, ALP, Col1α1, OCN,* and *OPN* in MSCs cultured in polystyrene plate, the DCB and periosteal bone scaffolds for 14 days. (D) Tube formation images in the phosphate buffer solution (PBS), DCB, periosteal bone scaffold, and vascular endothelial growth factor (VEGF) groups. (E, F) Quantitative analysis of loops (E) and intersection nodes (F) in D), three representative pictures were selected in each group for statistics. (G) H&E images revealed vascular infiltration 4 weeks after subcutaneous implantation in the DCB and periosteal bone scaffold groups. (H) Quantitative analysis of infiltrated vessels in the DCB and periosteal bone scaffold groups 4 weeks after subcutaneous implantation. DCB: Decellularized decalcified bone scaffold; P–B: Periosteal bone scaffold. Black triangle: blood vessel. Data are presented as mean ± SD (n = 4). (Scale bars are listed above; *: $P < 0.05$, **: $P < 0.01$, and ***: $P < 0.001$).

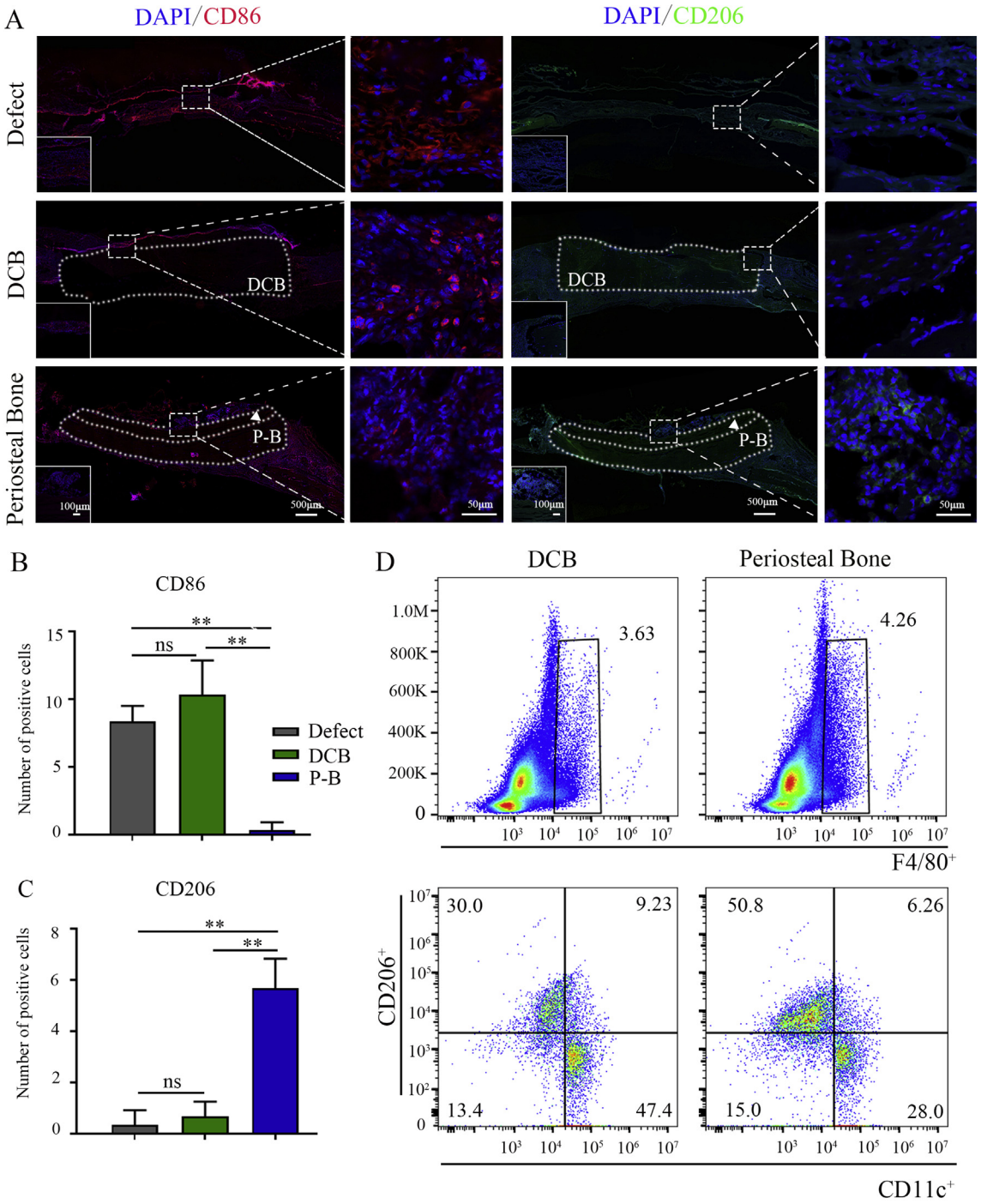

Fig. 7. The spatial form periosteal bone scaffold regulated macrophage polarization at an early stage of implantation of cranial defects. (A) Representative immunofluorescence images of CD86 (red) and CD206 (green) positive macrophages in empty defect, DCB, and periosteal bone scaffold groups at day 7 (green: CD206; red: CD86; blue: nucleus; the white dotted box represented the implanted scaffolds). (B, C) Quantitative analysis of CD86 (B) and CD206 (C) positive cells in the empty defect, DCB, and periosteal bone scaffold groups. (D) Representative flow cytometry analysis of F4/80, CD11c, and CD206 positive macrophages in the DCB and periosteal bone scaffold groups on day 7 of the subcutaneous embedding experiments. DCB: Decellularized decalcified bone. P–B: Periosteal bone scaffold. White triangle: periosteum. Data are presented as mean ± SD (n = 4). (Scale bars are listed above; *: $P < 0.05$, **: $P < 0.01$, and ***: $P < 0.001$).

To date, several studies have explored a similar structure. Danielle et al. constructed an artificial periosteum using polyethylene glycol hydrogel combined with MSCs and covered it on the surface of allogeneic bone [12]. And Khademhosseini et al. developed a microgrooved structure using polylactic acid-glycolic acid nanosheets to mimic the periosteal bone structure [11]. The tight attachment of the periosteum to the cortical bone is attributed to Sharpey fibers, which are nail-like structures in the periosteal fiber layer that insert into the cortical bone [34]; these designs were still far from the natural spatial structure. Yu et al. simulated the composite structure using an extracellular matrix derived from pre-osteoblasts and a gelatin methacryloyl hydrogel [35]. This scaffold had good biocompatibility, but the immunomodulatory role of the periosteum in bone healing was ignored. We acquired the periosteal bone complex via decellularization and demineralization, which preserved the natural composite structure, bioactive components and provided a framework for vessel penetration and osteogenesis differentiation. It also

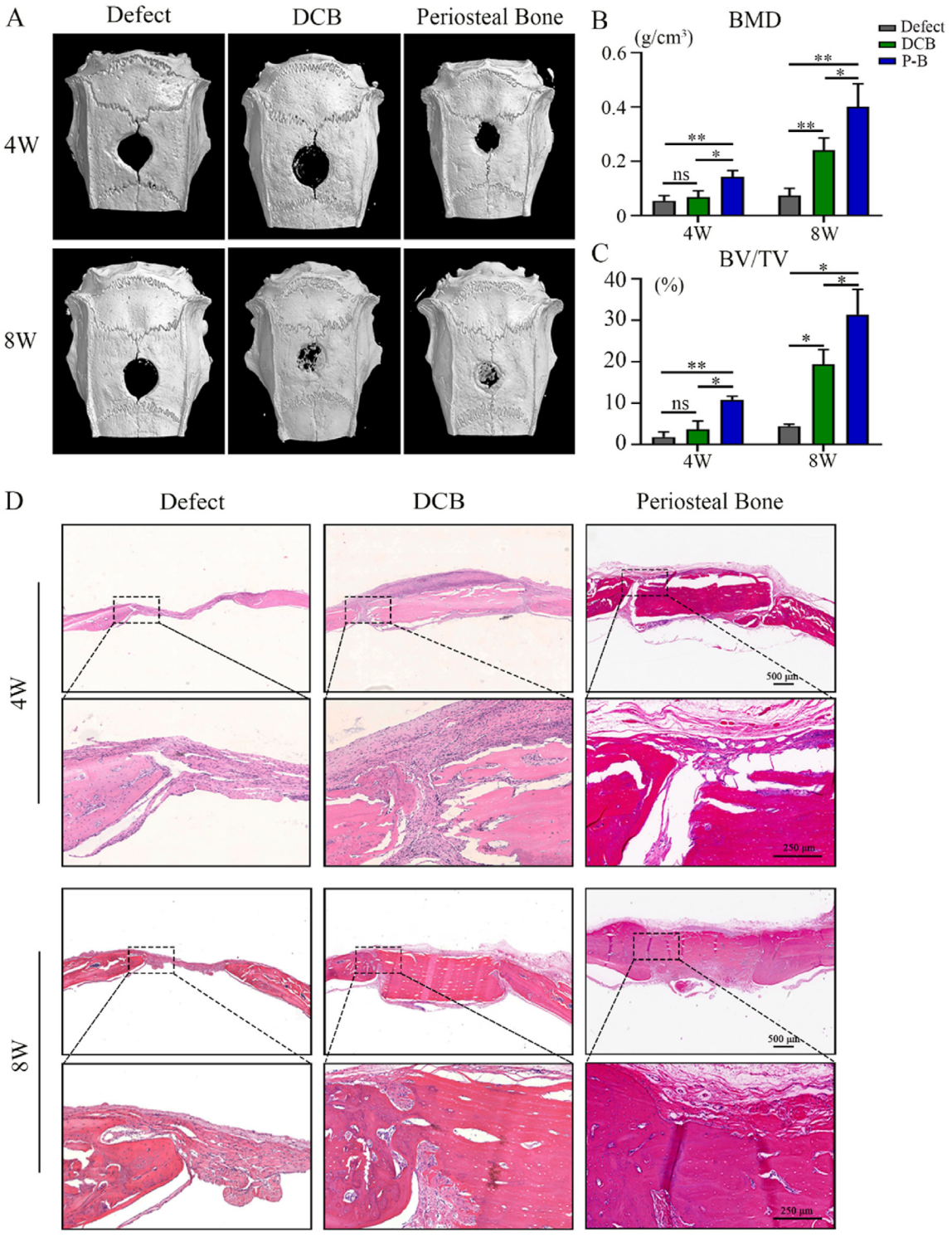

Fig. 8. The spatial form periosteal bone scaffold promoted to achieve good bone healing. (A) Mineralization of the calvarial defects evaluated by micro-CT 4 and 8 weeks after implantation. (B, C) Quantitative analysis of the BMD (B) and BV/TV (C) of the regenerated bone 4 and 8 weeks after implantation. (D) H&E staining of the calvarial defects 4 and 8 weeks after implantation. High magnification images of the regions highlighted by the black box are shown below. DCB: Decellularized decalcified bone; P–B: Periosteal bone scaffold. Data are presented as mean ± SD (n = 4). (Scale bars are listed above; *: $P < 0.05$, **: $P < 0.01$, and ***: $P < 0.001$).

participated in macrophage regulation at the damaged areas and provided positive feedback for subsequent bone healing.

For the preparation process, a literature search found few reports of acellular cortical bone scaffolds. Ko et al. once performed rat calvaria decellularization using a solution containing 0.5% SDS and 0.1% ammonium hydroxide for 3 weeks [36]. Our group previously reported the preparation of the periosteum scaffold using 2% Triton X-100 for 12 h and 1% SDS for 2 h [26]. By combining these parameters, the periosteal bone scaffold was decellularized with a mild, two-step protocol. After demineralization, 1% Triton X-100 was used to lyse cells for 12 h, and then treated with 1% SDS for 2 h; these steps helped to remove cellular components in the the periosteum part. As the cortical bone part was more compact, we wrapped the periosteum with a barrier membrane to expose cortical bone for a continued 34 h of 1% SDS treatment. The

preparation of periosteal bone scaffolds was comprehensively tested by H&E, DNA contents, and fragment sizes evaluation, all of which met the standards of complete decellularization.

Two major bioactive components (collagens and GAGs) in the periosteal bone scaffold were evaluated. Collagens are important components of the periosteum and bone [33], the contents in the periosteum decreased after treatment, but the difference was not significant. Compared with the previously reported periosteum protocol, the duration of SDS treatment in this study was longer, which might have influenced the decrease in collagen contents [37,38]. GAGs play a critical role in the preservation of biological growth factors [39]. Although decreased amounts of GAGs were observed both in the periosteum and cortical bone parts, these trends were consistent with previous reports, which might be due to their high sensitivity to detergent solutions [26,40]. Structurally, SEM observations demonstrated that the Sharpey fibers remained intact after treatment, which was a core indicator for the successful preparation of spatial form periosteal bone scaffolds. The periosteal collagen was well preserved, and the distribution was more orderly after treatment. Studies have reported that the distribution of periosteal collagen is consistent with the preferential direction of bone remodeling [41,42]. Therefore, the orderly distribution of periosteal collagen might be conducive to bone healing. In addition, pore-like structures were observed in the subperiosteal bone, which might facilitate the penetration of blood vessels.

Mechanical and nanoindentation tests indicated that the periosteum and cortical bone part in the periosteal bone scaffold had different mechanical properties and that Young's modulus of periosteum was considerably lower than that of the cortical bone. Recently, stiffness has attracted increasing attention owing to its important role in cell morphology, cell function, and mechanisms related to the occurrence of diseases [2,43,44]. Numbers of studies have reported that simply increasing the stiffness of substitutes without any additional factors can promote osteogenic differentiation of MSCs [2,45]. However, in the regulation of macrophages, stiff matrices tend to induce M1 polarization, while soft matrices are conducive to M2 transformation [22,46]. This may be the reason that traditional rigid inorganic biomaterials have clear advantages in osteogenesis, but difficult to realize the timely conversion of M1-to-M2 in early bone repair. In this study, BMMs seeded on composite periosteal bone scaffolds exhibited less expression of M1 macrophage-related markers, a preliminary investigation on the mechanism of how stiffness affects macrophage phenotypes was thus conducted. Macrophages mainly perceived stiffness through integrins and adhesion molecules on the cell surface [47,48], which connect to the cytoskeleton (actin, microtubules or intermediate filaments) or the subcellular structures [49,50]. The phenotype and function of macrophages were further regulated by transcription factors (e.g., YAP/TAZ, NF-κB) and epigenetic modifications [51,52]. Actin plays an important role in the macrophage mechanical signal transduction, Nikhil Jain et al. used 3D micropores and 2D micropatterns to limit the spread of macrophages, which inhibited the inflammatory gene expression profile by reducing actin polymerization [53]. Evidence further showed that YAP (a mediator of mechanotransduction) could reprogram macrophage phenotypes in many diseases [54–56]. The results in this study indicated that YAP activity might be related to stiffness, and inhibition of actin-mediated nuclear translocation of YAP had the potential for inflammatory suppression. Wendy F. Liu et al. obtained a similar conclusion supporting this hypothesis, and they found that matrix stiffness tuned the macrophage inflammatory response through the transcriptional coactivator YAP mediated by actin polymerization [25].

The spatial form periosteal bone scaffold realized M1-to-M2 conversion in the early stage of bone healing, which provided a supportive microenvironment for subsequent osteogenesis and vascularization. Studies have shown that M2 macrophages secrete a higher amount of BMP-2 than M0 or M1 macrophages [57], which can activate Smad1 and then promote the nuclear transfer of RUNX-2, thereby up-regulating the expression of osteogenic genes such as ALP and OCN in osteogenic precursor cells [58,59]. Gene expression analysis indicated that the periosteal bone scaffold promoted osteogenic differentiation; this was also supported by the presence of relevant proteins that provided a suitable osteogenic and mineralization microenvironment. Angiogenesis mainly includes the process of sprouting, anastomosis, and maturation [60]. M2 macrophages play an important role in the formation of blood vessels, which can promote germination by secreting high levels of MMP-9 and can also promote PDGF-BB to participate in anastomosis to mature [18]. Hashimoto et al. reported that neovascularization was achieved 6 months after subcutaneous implantation of decellularized bone matrix [61]. In contrast, clear vascular infiltration was observed in the fourth week in this study, and the infiltrating blood vessels were mainly distributed at the subperiosteal bone, where more pore-like structures were shown by SEM. Vascular infiltration might also be related to proteins that promote angiogenesis and regulate blood vessel diameter or structure. Finally, transplantation of the periosteal bone scaffold showed newly formed bone in vivo, and the underlying mechanism might be attributed to the bioactive components, complete structure, related functional proteins, and macrophage regulation of the periosteal bone scaffold [62–64].

However, this study still had several limitations. First, a preliminary study on the connection between actin-mediated YAP translocation and macrophage phenotypes was conducted; its precise mechanism requires more conclusive studies. Second, proteins that promoted osteogenesis and angiogenesis were detected by mass spectrometry, but the specific mechanisms remain unclear and require further investigation. Third, studies could be performed to test the periosteal bone scaffold in large animal models for future clinical application. In general, the preparation of periosteal bone scaffold provide new ideas for the repair of bone defects and also provide references for the preparation and application of similar complex physiological structures, such as cartilage-bone complex. The goal of decellularization is to promote host cell infiltration and ECM remodeling and ultimately achieve transplantation replacement [65]. Porcine-derived decellularized materials have abundant sources, there will be more forms of ECM-derived materials in the future [66], such as surface coatings, cell sheets, and polymer-coupled modified decellularized organs, to adapt to different clinical environments and expand the scope of potential clinical applications. And we also look forward to the application and success of more valuable decellularized materials in clinical orthopaedical patients, not limited to animal models.

5. Conclusion

The preparation of spatial form periosteal bone scaffold has achieved the complete retention of the composite structures and good reservation of bioactive components. Combined with the excellent osteogenesis and vascularization characteristics, the periosteal bone scaffold realized the timely M1-to-M2 conversion in early bone healing and promoted the subsequent regeneration, providing a new strategy for the clinical treatment of severe bone defects.

CRediT authorship contribution statement

Chenchen Zhao, Pengcheng Qiu, and Mobai Li: Conceptualization, Methodology, Data Curation, and Writing-Original Draft; **Kaiyu Liang and Zhibin Tang**: Methodology and Data Curation; **Pengfei Chen and Jianfeng Zhang**: Formal analysis; **Shunwu Fan and Xianfeng Lin**: Supervision, Project administration, Funding acquisition, and Writing - Review & Editing.

Funding

This study was supported by the National Key R&D Program of China (No. 2020YFC1107104), National Natural Science Foundation of China (No. 82072414), Key Research and Development Plan in Zhejiang Province (No. 2020C03043 and No. 2020C03041), Zhejiang Province

Medical and Health Science and Technology Project-Provincial and Ministry Co-construction Major Project (No. WKJ-ZJ-1906), Public Projects of Zhejiang Province (LGF19H060013 and LGF21H060005), Innovative Talent Support Program Project of Zhejiang Provincial Health Commission (No. 2021433298), Wenzhou major science and technology project (2018ZY015), Hangzhou Qianjiang Distinguished Expert and Zhejiang Provincial Program for the cultivation of high-level innovative health talents, China.

Declaration of competing interest

The authors declare that they have no known competing financial interests or personal relationships that could have appeared to influence the work reported in this paper.

Appendix A. Supplementary data

Supplementary data to this article can be found online at https://doi.org/10.1016/j.mtbio.2021.100142.

References

[1] A. Hertz, I.J. Bruce, Inorganic materials for bone repair or replacement applications, Nanomedicine 2 (6) (2007) 899–918, https://doi.org/10.2217/17435889.2.6.899 (Lond).
[2] A.J. Engler, S. Sen, H.L. Sweeney, D.E. Discher, Matrix elasticity directs stem cell lineage specification, Cell 126 (4) (2006) 677–689, https://doi.org/10.1016/j.cell.2006.06.044.
[3] J.M. Sadowska, M.P. Ginebra, Inflammation and biomaterials: role of the immune response in bone regeneration by inorganic scaffolds, J. Mater. Chem. B 8 (41) (2020) 9404–9427, https://doi.org/10.1039/d0tb01379j.
[4] H.D. Kim, S. Amirthalingam, S.L. Kim, S.S. Lee, J. Rangasamy, N.S. Hwang, Biomimetic materials and fabrication approaches for bone tissue engineering, Adv. Healthc Mater 6 (23) (2017), https://doi.org/10.1002/adhm.201700612.
[5] L. Bai, Y. Liu, Z. Du, Z. Weng, W. Yao, X. Zhang, X. Huang, X. Yao, R. Crawford, R. Hang, D. Huang, B. Tang, Y. Xiao, Differential effect of hydroxyapatite nano-particle versus nano-rod decorated titanium micro-surface on osseointegration, Acta Biomater. 76 (2018) 344–358, https://doi.org/10.1016/j.actbio.2018.06.023.
[6] T. Li, M. Peng, Z. Yang, X. Zhou, Y. Deng, C. Jiang, M. Xiao, J. Wang, 3D-printed IFN-gamma-loading calcium silicate-beta-tricalcium phosphate scaffold sequentially activates M1 and M2 polarization of macrophages to promote vascularization of tissue engineering bone, Acta Biomater. 71 (2018) 96–107, https://doi.org/10.1016/j.actbio.2018.03.012.
[7] P. Qiu, M. Li, K. Chen, B. Fang, P. Chen, Z. Tang, X. Lin, S. Fan, Periosteal matrix-derived hydrogel promotes bone repair through an early immune regulation coupled with enhanced angio- and osteogenesis, Biomaterials 227 (2020) 119552, https://doi.org/10.1016/j.biomaterials.2019.119552.
[8] B.J. Hurtgen, C.L. Ward, K. Garg, B.E. Pollot, S.M. Goldman, T.O. McKinley, J.C. Wenke, B.T. Corona, Severe muscle trauma triggers heightened and prolonged local musculoskeletal inflammation and impairs adjacent tibia fracture healing, J. Musculoskelet. Neuronal Interact. 16 (2) (2016) 122–134.
[9] K. Schmidt-Bleek, H. Schell, J. Lienau, N. Schulz, P. Hoff, M. Pfaff, G. Schmidt, C. Martin, C. Perka, F. Buttgereit, H.D. Volk, G. Duda, Initial immune reaction and angiogenesis in bone healing, J. Tissue Eng. Regen. Med. 8 (2) (2014) 120–130, https://doi.org/10.1002/term.1505.
[10] C.J. Hauser, X. Zhou, P. Joshi, M.A. Cuchens, P. Kregor, M. Devidas, R.J. Kennedy, G.V. Poole, J.L. Hughes, The immune microenvironment of human fracture/soft-tissue hematomas and its relationship to systemic immunity, J. Trauma. 42 (5) (1997) 895–903, https://doi.org/10.1097/00005373-199705000-00021, discussion 903-4.
[11] X. Shi, T. Fujie, A. Saito, S. Takeoka, Y. Hou, Y. Shu, M. Chen, H. Wu, A. Khademhosseini, Periosteum-mimetic structures made from freestanding microgrooved nanosheets, Adv. Mater. 26 (20) (2014) 3290–3296, https://doi.org/10.1002/adma.201305804.
[12] M.D. Hoffman, C. Xie, X. Zhang, D.S. Benoit, The effect of mesenchymal stem cells delivered via hydrogel-based tissue engineered periosteum on bone allograft healing, Biomaterials 34 (35) (2013) 8887–8898, https://doi.org/10.1016/j.biomaterials.2013.08.005.
[13] J. Shi, J. Sun, W. Zhang, H. Liang, Q. Shi, X. Li, Y. Chen, Y. Zhuang, J. Dai, Demineralized bone matrix scaffolds modified by CBD-SDF-1alpha promote bone regeneration via recruiting endogenous stem cells, ACS Appl. Mater. Interfaces 8 (41) (2016) 27511–27522, https://doi.org/10.1021/acsami.6b08685.
[14] S. Karaoglu, A. Baktir, S. Kabak, H. Arasi, Experimental repair of segmental bone defects in rabbits by demineralized allograft covered by free autogenous periosteum, Injury 33 (8) (2002) 679–683, https://doi.org/10.1016/s0020-1383(02)00086-4.
[15] O. Duchamp de Lageneste, A. Julien, R. Abou-Khalil, G. Frangi, C. Carvalho, N. Cagnard, C. Cordier, S.J. Conway, C. Colnot, Periosteum contains skeletal stem cells with high bone regenerative potential controlled by Periostin, Nat. Commun. 9 (1) (2018) 773, https://doi.org/10.1038/s41467-018-03124-z.
[16] C.S. Bahney, R.L. Zondervan, P. Allison, A. Theologis, J.W. Ashley, J. Ahn, T. Miclau, R.S. Marcucio, K.D. Hankenson, Cellular biology of fracture healing, J. Orthop. Res. 37 (1) (2019) 35–50, https://doi.org/10.1002/jor.24170.
[17] J. Loffler, F.A. Sass, S. Filter, A. Rose, A. Ellinghaus, G.N. Duda, A. Dienelt, Compromised bone healing in aged rats is associated with impaired M2 macrophage function, Front. Immunol. 10 (2019) 2443, https://doi.org/10.3389/fimmu.2019.02443.
[18] K.L. Spiller, R.R. Anfang, K.J. Spiller, J. Ng, K.R. Nakazawa, J.W. Daulton, G. Vunjak-Novakovic, The role of macrophage phenotype in vascularization of tissue engineering scaffolds, Biomaterials 35 (15) (2014) 4477–4488, https://doi.org/10.1016/j.biomaterials.2014.02.012.
[19] G. Rawadi, B. Vayssiere, F. Dunn, R. Baron, S. Roman-Roman, BMP-2 controls alkaline phosphatase expression and osteoblast mineralization by a Wnt autocrine loop, J. Bone Miner. Res. 18 (10) (2003) 1842–1853, https://doi.org/10.1359/jbmr.2003.18.10.1842.
[20] X. Liu, M. Chen, J. Luo, H. Zhao, X. Zhou, Q. Gu, H. Yang, X. Zhu, W. Cui, Q. Shi, Immunopolarization-regulated 3D printed-electrospun fibrous scaffolds for bone regeneration, Biomaterials 276 (2021) 121037, https://doi.org/10.1016/j.biomaterials.2021.121037.
[21] C. Yang, F.W. DelRio, H. Ma, A.R. Killaars, L.P. Basta, K.A. Kyburz, K.S. Anseth, Spatially patterned matrix elasticity directs stem cell fate, Proc. Natl. Acad. Sci. U. S. A. 113 (31) (2016) E4439–E4445, https://doi.org/10.1073/pnas.1609731113.
[22] R. Sridharan, B. Cavanagh, A.R. Cameron, D.J. Kelly, F.J. O'Brien, Material stiffness influences the polarization state, function and migration mode of macrophages, Acta Biomater. 89 (2019) 47–59, https://doi.org/10.1016/j.actbio.2019.02.048.
[23] B. Trappmann, J.E. Gautrot, J.T. Connelly, D.G. Strange, Y. Li, M.L. Oyen, M.A. Cohen Stuart, H. Boehm, B. Li, V. Vogel, J.P. Spatz, F.M. Watt, W.T. Huck, Extracellular-matrix tethering regulates stem-cell fate, Nat. Mater. 11 (7) (2012) 642–649, https://doi.org/10.1038/nmat3339.
[24] J. Xie, M. Bao, X. Hu, W.J.H. Koopman, W.T.S. Huck, Energy expenditure during cell spreading influences the cellular response to matrix stiffness, Biomaterials 267 (2021) 120494, https://doi.org/10.1016/j.biomaterials.2020.120494.
[25] V.S. Meli, H. Atcha, P.K. Veerasubramanian, R.R. Nagalla, T.U. Luu, E.Y. Chen, C.F. Guerrero-Juarez, K. Yamaga, W. Pandori, J.Y. Hsieh, T.L. Downing, D.A. Fruman, M.B. Lodoen, M.V. Plikus, W. Wang, W.F. Liu, YAP-mediated mechanotransduction tunes the macrophage inflammatory response, Sci. Adv. 6 (49) (2020), https://doi.org/10.1126/sciadv.abb8471.
[26] K. Chen, X. Lin, Q. Zhang, J. Ni, J. Li, J. Xiao, Y. Wang, Y. Ye, L. Chen, K. Jin, L. Chen, Decellularized periosteum as a potential biologic scaffold for bone tissue engineering, Acta Biomater. 19 (2015) 46–55, https://doi.org/10.1016/j.actbio.2015.02.020.
[27] X. Lin, C. Zhao, P. Zhu, J. Chen, H. Yu, Y. Cai, Q. Zhang, A. Qin, S. Fan, Periosteum extracellular-matrix-mediated acellular mineralization during bone formation, Adv. Healthc Mater 7 (4) (2018), https://doi.org/10.1002/adhm.201700660.
[28] P.F. Gratzer, R.D. Harrison, T. Woods, Matrix alteration and not residual sodium dodecyl sulfate cytotoxicity affects the cellular repopulation of a decellularized matrix, Tissue Eng. 12 (10) (2006) 2975–2983, https://doi.org/10.1089/ten.2006.12.2975.
[29] P. Abreu, G.N. Marzuca-Nassr, S.M. Hirabara, R. Curi, Experimental model of skeletal muscle laceration in rats, Methods Mol. Biol. 1735 (2018) 397–401, https://doi.org/10.1007/978-1-4939-7614-0_27.
[30] S. Dupont, L. Morsut, M. Aragona, E. Enzo, S. Giulitti, M. Cordenonsi, F. Zanconato, J. Le Digabel, M. Forcato, S. Bicciato, N. Elvassore, S. Piccolo, Role of YAP/TAZ in mechanotransduction, Nature 474 (7350) (2011) 179–183, https://doi.org/10.1038/nature10137.
[31] J.G. Baldwin, F. Wagner, L.C. Martine, B.M. Holzapfel, C. Theodoropoulos, O. Bas, F.M. Savi, C. Werner, E.M. De-Juan-Pardo, D.W. Hutmacher, Periosteum tissue engineering in an orthotopic in vivo platform, Biomaterials 121 (2017) 193–204, https://doi.org/10.1016/j.biomaterials.2016.11.016.
[32] G.C. Ingavle, M. Gionet-Gonzales, C.E. Vorwald, L.K. Bohannon, K. Clark, L.D. Galuppo, J.K. Leach, Injectable mineralized microsphere-loaded composite hydrogels for bone repair in a sheep bone defect model, Biomaterials 197 (2019) 119–128, https://doi.org/10.1016/j.biomaterials.2019.01.005.
[33] X. Cai, H. Follet, L. Peralta, M. Gardegaront, D. Farlay, R. Gauthier, B. Yu, E. Gineyts, C. Olivier, M. Langer, A. Gourrier, D. Mitton, F. Peyrin, Q. Grimal, P. Laugier, Anisotropic elastic properties of human femoral cortical bone and relationships with composition and microstructure in elderly, Acta Biomater. 90 (2019) 254–266, https://doi.org/10.1016/j.actbio.2019.03.043.
[34] S. Hirashima, K. Ohta, T. Kanazawa, K. Uemura, A. Togo, M. Yoshitomi, S. Okayama, J. Kusukawa, K. Nakamura, Anchoring structure of the calvarial periosteum revealed by focused ion beam/scanning electron microscope tomography, Sci. Rep. 5 (2015) 17511, https://doi.org/10.1038/srep17511.
[35] Y. Yu, Y. Wang, W. Zhang, H. Wang, J. Li, L. Pan, F. Han, B. Li, Biomimetic periosteum-bone substitute composed of preosteoblast-derived matrix and hydrogel for large segmental bone defect repair, Acta Biomater. 113 (2020) 317–327, https://doi.org/10.1016/j.actbio.2020.06.030.
[36] D.J. Lee, S. Diachina, Y.T. Lee, L. Zhao, R. Zou, N. Tang, H. Han, X. Chen, C.C. Ko, Decellularized bone matrix grafts for calvaria regeneration, J. Tissue Eng. 7 (2016), https://doi.org/10.1177/2041731416680306, 2041731416680306.
[37] S.E. Gilpin, J.P. Guyette, G. Gonzalez, X. Ren, J.M. Asara, D.J. Mathisen, J.P. Vacanti, H.C. Ott, Perfusion decellularization of human and porcine lungs: bringing the matrix to clinical scale, J. Heart Lung Transplant. 33 (3) (2014) 298–308, https://doi.org/10.1016/j.healun.2013.10.030.

[38] K. Theodoridis, J. Muller, R. Ramm, K. Findeisen, B. Andree, S. Korossis, A. Haverich, A. Hilfiker, Effects of combined cryopreservation and decellularization on the biomechanical, structural and biochemical properties of porcine pulmonary heart valves, Acta Biomater. 43 (2016) 71–77, https://doi.org/10.1016/j.actbio.2016.07.013.

[39] M. Yuan, C.W. Yeung, Y.Y. Li, H. Diao, K.M.C. Cheung, D. Chan, K. Cheah, P.B. Chan, Effects of nucleus pulposus cell-derived acellular matrix on the differentiation of mesenchymal stem cells, Biomaterials 34 (16) (2013) 3948–3961, https://doi.org/10.1016/j.biomaterials.2013.02.004.

[40] C. Zhao, S. Wang, G. Wang, M. Su, L. Song, J. Chen, S. Fan, X. Lin, Preparation of decellularized biphasic hierarchical myotendinous junction extracellular matrix for muscle regeneration, Acta Biomater. 68 (2018) 15–28, https://doi.org/10.1016/j.actbio.2017.12.035.

[41] J. Foolen, C. van Donkelaar, N. Nowlan, P. Murphy, R. Huiskes, K. Ito, Collagen orientation in periosteum and perichondrium is aligned with preferential directions of tissue growth, J. Orthop. Res. 26 (9) (2008) 1263–1268, https://doi.org/10.1002/jor.20586.

[42] A. Petersen, A. Princ, G. Korus, A. Ellinghaus, H. Leemhuis, A. Herrera, A. Klaumunzer, S. Schreivogel, A. Woloszyk, K. Schmidt-Bleek, S. Geissler, I. Heschel, G.N. Duda, A biomaterial with a channel-like pore architecture induces endochondral healing of bone defects, Nat. Commun. 9 (1) (2018) 4430, https://doi.org/10.1038/s41467-018-06504-7.

[43] J. Nam, J. Johnson, J.J. Lannutti, S. Agarwal, Modulation of embryonic mesenchymal progenitor cell differentiation via control over pure mechanical modulus in electrospun nanofibers, Acta Biomater. 7 (4) (2011) 1516–1524, https://doi.org/10.1016/j.actbio.2010.11.022.

[44] M. Egeblad, M.G. Rasch, V.M. Weaver, Dynamic interplay between the collagen scaffold and tumor evolution, Curr. Opin. Cell Biol. 22 (5) (2010) 697–706, https://doi.org/10.1016/j.ceb.2010.08.015.

[45] A. Cipitria, K. Boettcher, S. Schoenhals, D.S. Garske, K. Schmidt-Bleek, A. Ellinghaus, A. Dienelt, A. Peters, M. Mehta, C.M. Madl, N. Huebsch, D.J. Mooney, G.N. Duda, In-situ tissue regeneration through SDF-1alpha driven cell recruitment and stiffness-mediated bone regeneration in a critical-sized segmental femoral defect, Acta Biomater. 60 (2017) 50–63, https://doi.org/10.1016/j.actbio.2017.07.032.

[46] T. Okamoto, Y. Takagi, E. Kawamoto, E.J. Park, H. Usuda, K. Wada, M. Shimaoka, Reduced substrate stiffness promotes M2-like macrophage activation and enhances peroxisome proliferator-activated receptor gamma expression, Exp. Cell Res. 367 (2) (2018) 264–273, https://doi.org/10.1016/j.yexcr.2018.04.005.

[47] B. Geiger, A. Bershadsky, R. Pankov, K.M. Yamada, Transmembrane crosstalk between the extracellular matrix–cytoskeleton crosstalk, Nat. Rev. Mol. Cell Biol. 2 (11) (2001) 793–805, https://doi.org/10.1038/35099066.

[48] D.E. Leckband, Q. le Duc, N. Wang, J. de Rooij, Mechanotransduction at cadherin-mediated adhesions, Curr. Opin. Cell Biol. 23 (5) (2011) 523–530, https://doi.org/10.1016/j.ceb.2011.08.003.

[49] J. Eyckmans, T. Boudou, X. Yu, C.S. Chen, A hitchhiker's guide to mechanobiology, Dev. Cell 21 (1) (2011) 35–47, https://doi.org/10.1016/j.devcel.2011.06.015.

[50] I. Dasgupta, D. McCollum, Control of cellular responses to mechanical cues through YAP/TAZ regulation, J. Biol. Chem. 294 (46) (2019) 17693–17706, https://doi.org/10.1074/jbc.REV119.007963.

[51] J. Benditt, Patented remedy, Sci. Am. 258 (5) (1988) 32–34, https://doi.org/10.1038/scientificamerican0588-32.

[52] K. Otsuka, M. Mizuno, K. Kagawa, K. Kashima, S. Ohkuma, Presence of a Vicia unijuga lectin-binding (Vgu) glycoprotein with Thomsen-Friedenreich (T) activity and Vgu glycoproteins in human primary hepatocellular carcinoma, Int. J. Biochem. 24 (9) (1992) 1407–1419, https://doi.org/10.1016/0020-711x(92)90066-a.

[53] N. Jain, V. Vogel, Spatial confinement downsizes the inflammatory response of macrophages, Nat. Mater. 17 (12) (2018) 1134–1144, https://doi.org/10.1038/s41563-018-0190-6.

[54] T. Panciera, L. Azzolin, M. Cordenonsi, S. Piccolo, Mechanobiology of YAP and TAZ in physiology and disease, Nat. Rev. Mol. Cell Biol. 18 (12) (2017) 758–770, https://doi.org/10.1038/nrm.2017.87.

[55] M.M. Mia, D.M. Cibi, S.A.B. Abdul Ghani, W. Song, N. Tee, S. Ghosh, J. Mao, E.N. Olson, M.K. Singh, YAP/TAZ deficiency reprograms macrophage phenotype and improves infarct healing and cardiac function after myocardial infarction, PLoS Biol. 18 (12) (2020), e3000941, https://doi.org/10.1371/journal.pbio.3000941.

[56] X. Zhou, W. Li, S. Wang, P. Zhang, Q. Wang, J. Xiao, C. Zhang, X. Zheng, X. Xu, S. Xue, L. Hui, H. Ji, B. Wei, H. Wang, YAP aggravates inflammatory bowel disease by regulating M1/M2 macrophage polarization and gut microbial homeostasis, Cell Rep. 27 (4) (2019) 1176–1189, https://doi.org/10.1016/j.celrep.2019.03.028, e5.

[57] Y. Zhang, T. Bose, R.E. Unger, J.A. Jansen, C.J. Kirkpatrick, J. van den Beucken, Macrophage type modulates osteogenic differentiation of adipose tissue MSCs, Cell Tissue Res. 369 (2) (2017) 273–286, https://doi.org/10.1007/s00441-017-2598-8.

[58] J. Munoz, N.S. Akhavan, A.P. Mullins, B.H. Arjmandi, Macrophage polarization and osteoporosis: a review, Nutrients 12 (10) (2020), https://doi.org/10.3390/nu12102999.

[59] J. Pajarinen, T. Lin, E. Gibon, Y. Kohno, M. Maruyama, K. Nathan, L. Lu, Z. Yao, S.B. Goodman, Mesenchymal stem cell-macrophage crosstalk and bone healing, Biomaterials 196 (2019) 80–89, https://doi.org/10.1016/j.biomaterials.2017.12.025.

[60] S.P. Herbert, D.Y. Stainier, Molecular control of endothelial cell behaviour during blood vessel morphogenesis, Nat. Rev. Mol. Cell Biol. 12 (9) (2011) 551–564, https://doi.org/10.1038/nrm3176.

[61] Y. Hashimoto, S. Funamoto, T. Kimura, K. Nam, T. Fujisato, A. Kishida, The effect of decellularized bone/bone marrow produced by high-hydrostatic pressurization on the osteogenic differentiation of mesenchymal stem cells, Biomaterials 32 (29) (2011) 7060–7067, https://doi.org/10.1016/j.biomaterials.2011.06.008.

[62] M. Kuljanin, C.F.C. Brown, M.J. Raleigh, G.A. Lajoie, L.E. Flynn, Collagenase treatment enhances proteomic coverage of low-abundance proteins in decellularized matrix bioscaffolds, Biomaterials 144 (2017) 130–143, https://doi.org/10.1016/j.biomaterials.2017.08.012.

[63] J. Jang, H.J. Park, S.W. Kim, H. Kim, J.Y. Park, S.J. Na, H.J. Kim, M.N. Park, S.H. Choi, S.H. Park, S.W. Kim, S.M. Kwon, P.J. Kim, D.W. Cho, 3D printed complex tissue construct using stem cell-laden decellularized extracellular matrix bioinks for cardiac repair, Biomaterials 112 (2017) 264–274, https://doi.org/10.1016/j.biomaterials.2016.10.026.

[64] Z. Lin, D. Shen, W. Zhou, Y. Zheng, T. Kong, X. Liu, S. Wu, P.K. Chu, Y. Zhao, J. Wu, K.M.C. Cheung, K.W.K. Yeung, Regulation of extracellular bioactive cations in bone tissue microenvironment induces favorable osteoimmune conditions to accelerate in situ bone regeneration, Bioact Mater 6 (8) (2021) 2315–2330, https://doi.org/10.1016/j.bioactmat.2021.01.018.

[65] Q. Yao, Y.W. Zheng, Q.H. Lan, L. Kou, H.L. Xu, Y.Z. Zhao, Recent development and biomedical applications of decellularized extracellular matrix biomaterials, Mater Sci Eng C Mater Biol Appl 104 (2019) 109942, https://doi.org/10.1016/j.msec.2019.109942.

[66] H. Xing, H. Lee, L. Luo, T.R. Kyriakides, Extracellular matrix-derived biomaterials in engineering cell function, Biotechnol. Adv. 42 (2020) 107421, https://doi.org/10.1016/j.biotechadv.2019.107421.